IET Radar, Sonar & Navigation

WILEY

The Institution of Engineering and Technology

ORIGINAL RESEARCH OPEN ACCESS

Experimental Evaluation of Range Disambiguation Methods Using Slow-Time Coding for Moving Target Indication

Jennifer Quirk[1] | Patrick McCormick[1] | Jonathan Owen[1] | Alfred Fontes[1,2] | Shannon Blunt[1]

[1]Radar Systems Lab (RSL), University of Kansas, Lawrence, Kansas, USA | [2]Integrated Electromagnetics, Circuits, and Systems (IECS) Lab, University of Virginia, Charlottesville, Virginia, USA

Correspondence: Jennifer Quirk (jennifer_quirk@ku.edu)

Received: 3 October 2025 | **Revised:** 28 February 2026 | **Accepted:** 18 March 2026

Keywords: adaptive signal processing | Doppler radar | mean square error methods | phase coding | radar signal processing | radar waveforms

ABSTRACT

Conventional pulse-Doppler radar processing suffers from range and velocity ambiguities due to the periodic nature of pulse repetition intervals (PRIs). Traditional disambiguation using the coincidence algorithm requires multiple coherent intervals with varying PRIs to resolve range and velocity ambiguities, leading to extended search timelines and inefficient use of transmitted energy. Slow-time coding (STC) is a well-established range disambiguation technique that applies a complex scalar to each pulse, enabling separation of scattering from different range intervals through decorrelation. This work evaluates both random and optimised STC sequences. A phase-only STC optimisation framework is introduced that reduces the sidelobe energy of range-folded scattering within a desired Doppler notch bandwidth when applying the Doppler matched filter. The design is found to be effective if the Doppler notch is small compared to the unambiguous Doppler extent. To address the shortcomings of conventional STC Doppler processing, an adaptive method called MR-RISR is also developed. When combined with STC, it iteratively estimates and isolates scattering from multiple range intervals by suppressing both range-folded and range-coincident sidelobe energy. MR-RISR operates on a single slow-time data snapshot, eliminating the need for training data or knowledge of the clutter + noise covariance, and achieves SINR performance comparable to that of the clairvoyant max-SINR filter. An open-air experiment was conducted to evaluate MR-RISR against conventional and max-SINR processing using both random and optimised STCs, with the latter shown to be necessary for Doppler matched filter processing to effectively suppress folded clutter energy. MR-RISR and max-SINR processing yield comparable performance for both random and optimised STC sequences, with MR-RISR providing enhanced sidelobe suppression of targets and exhibiting modest Doppler super-resolution.

1 | Introduction

A pulse-Doppler radar measures range and (radial) velocity of scattering by comparing the backscattered responses from multiple pulses transmitted at a pulse repetition frequency (PRF) (denoted f_{PRF}). The periodic nature of the transmission can introduce ambiguity when estimating the range and/or velocity of scatterers. For example, a scatterer will appear at a closer apparent range if its backscattered energy arrives after the transmission of the next pulse—referred to as range-folded or multiple-time-around scattering. Pulse-Doppler radars commonly operate in a moving target indication (MTI) mode with the objective of estimating and detecting target energy in the presence of system noise and undesired backscatter known as 'clutter.' Traditionally, disambiguation of a target's true range and velocity is achieved by acquiring multiple coherent processing intervals (CPIs) with distinct PRFs. Since the apparent range-velocity of an ambiguous target varies with PRF, the true

values can be resolved by comparing candidate range-velocities derived from each CPI—a process known as the coincidence algorithm [1]. Although effective in disambiguation, this technique extends search timelines and is inefficient in its utilisation of transmit energy.

Slow-time coding (STC) of pulses has emerged as a means to mitigate range-folded scattering by coding each pulse in a CPI with a complex scalar [2–16]. In doing so, returns from each range interval exhibit distinct Doppler signatures that decorrelate based on the selected segment of the slow-time sequence while retaining the unambiguous Doppler extent set by the PRF, that is, $f_D \in [-f_{PRF}/2, f_{PRF}/2]$. Therefore, STC is particularly useful in the case where scattering is slow-moving and possibly folded in range, as in high PRF applications [6, 13], weather radar [2, 5, 11, 14], and some applications of over-the-horizon radar [3, 4, 9]. Note that other range disambiguation techniques exist that leverage pulse-to-pulse waveform diversity but are considered distinct from STC as the underlying pulse modulation changes throughout the CPI (e.g., in [17, 18]).

Leveraging numerical optimisation techniques, STC sequences can be designed to improve radar performance for particular collection scenarios. In [7], STC sequences are optimised (in both phase and amplitude) to maximise the probability of detection of a signal in the presence of signal-independent, coloured-Gaussian noise, which was extended to phase-only STC optimisation in [8]. Similarly, the work in [16] jointly maximises target signal-to-inteference + noise ratio (SINR) and minimises the target estimation error bounds for signal-independent, coloured interference. In [12], SINR is maximised via STC optimisation in the presence of signal-dependent interference (i.e., clutter) from multiple range intervals. In these works, the STC optimisation incorporates a 'similarity constraint' that constrains the STC to be 'near' a reference code that is known to have a desirable ambiguity function. Alternatively in [15], phase-only STC sequences and associated slow-time tapering are optimised to improve the SINR of a tangentially moving target located in a desired range interval and corrupted by range-folded clutter and noise.

Separately, nonlinear processing methods can improve estimation of the Doppler spectrum for both standard and waveform-diverse transmissions [19]. For instance, [9] uses second-order blind identification (SOBI) with a space-time sample covariance matrix to suppress range-folded clutter. Additionally, the reiterative super-resolution (RISR) algorithm [20], originally applied to direction-of-arrival estimation, was experimentally demonstrated in an open-air environment to improve the spectral estimate in Doppler [21]. Moreover, due to similarities in the signal modelling, the RISR algorithm has been reformulated to encompass slow-time Doppler [21], fast-time space [22], and fast-time frequency [23] representations. RISR represents a specific instantiation of the reiterative minimum mean squared error (RMMSE) framework, wherein parameter estimation is achieved through the construction of a structured covariance matrix that leverages current estimates. The RMMSE framework has also been employed in the range [24] and joint range/Doppler dimensions [25], with open-air demonstration shown in [26]. Furthermore, the work in [10] performed an initial comparison between conventional, maximum SINR, and 'RISR-like' Doppler processing for range disambiguation using random binary and uniformly random STC sequences.

Recently, [27] derived a form of RISR that, when coupled with STC, adaptively estimates (and disambiguates) scattering arising from multiple range intervals. This multi-range RISR (MR-RISR) formulation leverages the unique Doppler STC phase progressions of each range interval to suppress cross-correlation sidelobe energy that would otherwise be present with conventional processing (i.e., Doppler matched filtering). Here, MR-RISR is evaluated for both random and optimised STC sequences and compared with conventional processing and maximum SINR filtering. For the optimised sequence, a phase-only STC design is presented that notches a prescribed region in Doppler for any number of range-folded Doppler regions. For this work, a stationary single-channel pulse-Doppler configuration is assumed; thus, the STC optimisation is defined to reduce folded sidelobe energy caused by zero-Doppler clutter.

These processing methods and STC sequences are evaluated both in simulation and an open-air data collect. An SINR analysis is performed for a representative clutter + noise scenario to demonstrate the benefits of STC optimisation and adaptive processing. It is shown that the optimised STC coupled with the optimal max-SINR filter achieves nearly 0 dB SINR loss within the optimised notch region and degrades outside this region. If the max-SINR solution is not feasible, optimised STC coupled with tapered matched filtering is shown to dramatically improve the SINR performance relative to a randomised STC. Further, MR-RISR is shown to achieve an SINR loss of only about 2 dB worse than the clairvoyant max-SINR solution (for both STCs) without any requirement of a clutter + noise estimate. For the open-air collection, a random STC and two optimised STCs with different notch bandwidths are encoded onto a linear frequency modulation (LFM) waveform pulse train designed to induce range-folding of scattering. Two non-STC CPIs with low and high PRFs were likewise collected to serve as ground truth and fully ambiguous control cases, respectively. It is shown that the optimised STC is needed when using conventional Doppler processing to reduce the folded clutter response, while both max-SINR and MR-RISR exhibit excellent range disambiguation for all STC cases, with the latter achieving additional sidelobe suppression and modest super-resolution.

2 | Slow-Time Coding (STC) Signal Model

Consider a pulse-Doppler radar transmitting a sequence of pulses at a uniform PRI denoted as $T_p = \frac{1}{f_{PRF}}$ within a coherent processing interval (CPI), where each pulse is modulated by the same complex baseband waveform $s(t)$ having pulse duration T and bandwidth B. The m^{th} pulse is rotated by a slow-time phase θ_m to produce the STC. Therefore, waveform modulation over the entire CPI can be expressed as

$$s_c(t) = \sum_m s(t - mT_p)e^{j\theta_m}. \quad (1)$$

For ground truth scattering response $x(\tau, f_D)$, the complex-valued (baseband) received signal over the entire CPI can be expressed via integration over all delay τ and Doppler $f_D = 2v/\lambda$ Hz (for radial velocity v and wavelength λ) as

$$y(t) = \int_{f_{D,min}}^{f_{D,max}} \int_{\tau_{min}}^{\tau_{max}} s_c(t-\tau; f_D) x(\tau, f_D) d\tau df_D + u(t). \quad (2)$$

Here $u(t)$ is a white complex-valued Gaussian noise process,

$$\begin{aligned} s_c(t; f_D) &= s_c(t) e^{j2\pi f_D t} \\ &= \sum_m s(t - mT_p) e^{j\theta_m} e^{j2\pi f_D t} \\ &= \sum_m s(t - mT_p; f_D) e^{j\theta_m} e^{j2\pi m f_D T_p} \end{aligned} \quad (3)$$

represents the Doppler-shifted transmission, and

$$s(t; f_D) = s(t) e^{j2\pi f_D t} \quad (4)$$

is the Doppler-shifted pulsed waveform. It is assumed that all significant scattering is contained within the intervals $\tau_{min} \le \tau \le \tau_{max}$ and $f_{D,min} \le f_D \le f_{D,max}$.

Using Equation (2), define the response from the m^{th} received interval as $y_m(\bar{t}) = y(\bar{t} + mT_p)$ for $0 \le \bar{t} \le T_p$, which yields

$$y_m(\bar{t}) = \int \int s_c(\bar{t} - (\tau - mT_p); f_D) x(\tau, f_D) d\tau df_D + u_m(\bar{t}) \quad (5)$$

for $u_m(\bar{t}) = u(\bar{t} + mT_p)$, with the integration limits in Equation (5) suppressed for brevity. Using Equation (3), we can then express Equation (5) as

$$\begin{aligned} y_m(\bar{t}) = \sum_{m'=0}^{m} \int \int & s(\bar{t} - (\tau + (m' - m)T_p); f_D) x(\tau, f_D) \\ & \times e^{j\theta_{m'}} e^{j2\pi m' f_D T_p} d\tau df_D + u_m(\bar{t}), \end{aligned} \quad (6)$$

where the summation terminates at m since it only depends on the current and previous pulses.

Multiple assumptions can be made to simplify the expression in Equation (6). First, assume the Doppler spread of scattering is small enough that fast-time Doppler effects are negligible over a pulse duration T (i.e., $s(t; f_D) \approx s(t)$ for $f_{D,min} \le f_D \le f_{D,max}$). Second, assume the scattering in $x(\tau, f_D)$ is contained within the first G range intervals (i.e., $\tau_{min} = 0 \le \tau \le \tau_{max} = GT_p$). Therefore, the summation can be redefined as being over range intervals rather than pulses. Further, defining $g = m - m' = 0, 1, ..., G-1$ as the range interval index and $0 \le \bar{\tau} \le T_p$ as the wrapped delay interval, the integration limits for τ can be split into a summation of G integrations over $\bar{\tau}$, where $\tau = \bar{\tau} + gT_p$. Consequently, Equation (6) becomes

$$\begin{aligned} y_m(\bar{t}) = \sum_{g=0}^{\min(G-1,m)} \int \int & s(\bar{t} - \bar{\tau}) x(\bar{\tau} + gT_p, f_D) \\ & \times e^{j\theta_{m-g}} e^{j2\pi(m-g) f_D T_p} d\bar{\tau} df_D + u_m(\bar{t}), \end{aligned} \quad (7)$$

where $\min(G-1, m)$ in the summation accounts for the transient period at the beginning of the CPI where there are no returns from further-out range intervals.

For G observable range intervals, $(G-1)$ fill pulses [28] are needed so that scattering from all G range intervals consistently superimpose for all pulses in the CPI. For a CPI of M pulses, a total of $M + G - 1$ pulses are transmitted to ensure that the M coherently processed pulses have returns from all G range intervals. Therefore, the $m = 0, 1, ..., G-2$ indexed pulses are the fill pulses, and the $m = G-1, G, ..., G+M-2$ indexed pulses comprise the CPI as illustrated in Figure 1 for $M = 4$ and $G = 3$.

Applying the matched filter to Equation (6), shown here in continuous time for ease of notation, provides the superimposed delay profile estimates for all G intervals over the wrapped delay interval $\bar{\tau}$ via

$$\begin{aligned} \hat{z}_m(\bar{\tau}) &= \int s^*(\bar{t} - \bar{\tau}) y_m(\bar{t}) d\bar{t} \\ &= \sum_{g=0}^{G-1} \int \tilde{x}_g(\bar{\tau}, f_D) e^{j\theta_{m-g}} e^{j2\pi(m-G+1) f_D T_p} df_D + \tilde{u}_m(\bar{\tau}) \end{aligned} \quad (8)$$

for $m = G-1, G, ..., G+M-2$. Here $\tilde{x}_g(\bar{\tau}, f_D)$ is the delay-Doppler scattering for the g^{th} range interval (i.e., $x(\bar{\tau} + gT_p, f_D)$) shaped by the autocorrelation function of $s(t)$, and $\tilde{u}_m(\bar{\tau})$ is the noise process shaped by the matched filter. For notational simplicity, a factor of $e^{j2\pi(G-1-g) f_D T_p}$ is subsumed into the scattering response $\tilde{x}_g(\bar{\tau}, f_D)$ to ensure the Doppler phase progression starts at zero phase for all range intervals (i.e., $2\pi(m - G + 1) f_D T_p$). This subsumed phase combines with the random phase of the backscattered scene and has no effect on subsequent estimation.

Since each of the $g = 0, 1, ..., G-1$ range intervals have a distinct STC structure, the $M \times 1$ Doppler steering vector for the g^{th} range interval can be defined (per [28]) according to the argument of the complex exponential from Equation (8) as

$$\mathbf{v}_g(f_D) = \mathbf{v}(f_D) \odot (\mathbf{T}_g \mathbf{d}(\theta)), \quad (9)$$

where $\odot$ is the Hadamard product. The steering vector $\mathbf{v}(f_D)$ has the standard Vandermonde form

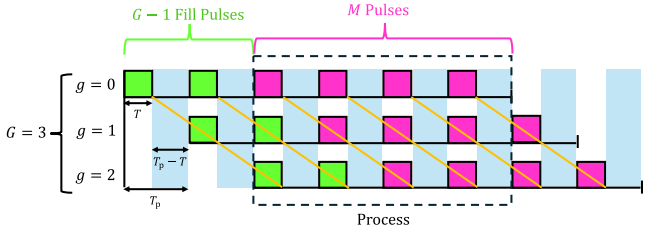

FIGURE 1 | Illustration of fill pulses and overlapped range intervals. Each additional delay of T_p shifts the observed pulses through the specified range intervals.

$$\mathbf{v}(f_{\mathrm{D}}) = \begin{bmatrix} 1 & e^{j2\pi(1)f_{\mathrm{D}}T_{\mathrm{p}}} & \ldots & e^{j2\pi(M-1)f_{\mathrm{D}}T_{\mathrm{p}}} \end{bmatrix}^T, \tag{10}$$

for $(\bullet)^T$ denoting vector transpose, $\mathbf{d}(\theta)$ is the $(G+M-1)\times 1$ phase vector that collects the STC sequence as

$$\mathbf{d}(\theta) = \begin{bmatrix} e^{j\theta_0} & e^{j\theta_1} & \ldots & e^{j\theta_{G+M-2}} \end{bmatrix}^T \tag{11}$$

for $\theta = [\theta_0, \theta_1, \ldots, \theta_{M+G-2}]^T$, and

$$\mathbf{T}_g = \begin{bmatrix} \mathbf{0}_{M\times(G-1-g)} & \mathbf{I}_{M\times M} & \mathbf{0}_{M\times g} \end{bmatrix} \tag{12}$$

is a $M \times (G+M-1)$ selection matrix that extracts the components in $\mathbf{d}(\theta)$ corresponding to returns from the g^{th} range interval, with $\mathbf{I}_{M\times M}$ the $M \times M$ identity matrix and $\mathbf{0}_{M\times g}$ a zeros matrix. The implication of Equation (9) is a unique Doppler manifold associated with each range interval g, thereby enabling separability of desired scattering from each range interval.

3 | Range Disambiguation Methods Using STC

In a moving target indication (MTI) context, the desired scattering consists of radial movers (e.g., vehicles), while undesired scattering (i.e., 'clutter') comprises all stationary (e.g., the ground) or quasi-stationary (e.g., swaying trees/bushes) scattering. Therefore, $\tilde{x}_g(\bar{\tau}, f_{\mathrm{D}})$ can be separated into subsequent clutter (subscript 'c') and target (subscript 't') components as

$$\tilde{x}_g(\bar{\tau}, f_{\mathrm{D}}) = \tilde{x}_{\mathrm{t},g}(\bar{\tau}, f_{\mathrm{D}}) + \tilde{x}_{\mathrm{c},g}(\bar{\tau}, f_{\mathrm{D}}). \tag{13}$$

Collecting M pulses of Equation (8) into $M \times 1$ vector $\mathbf{z}(\bar{\tau})$, we can express this slow-time data vector via a superposition of clutter, target, and noise components for each range interval as

$$\mathbf{z}(\bar{\tau}) = \sum_{g=0}^{G-1} \mathbf{z}_{\mathrm{t},g}(\bar{\tau}) + \sum_{g=0}^{G-1} \mathbf{z}_{\mathrm{c},g}(\bar{\tau}) + \mathbf{u}(\bar{\tau}). \tag{14}$$

Here $\mathbf{u}(\bar{\tau})$ is the $M \times 1$ collection of noise samples from Equation (8),

$$\mathbf{z}_{\mathrm{t},g}(\bar{\tau}) = \int \tilde{x}_{\mathrm{t},g}(\bar{\tau}, f_{\mathrm{D}})\mathbf{v}_g(f_{\mathrm{D}})df_{\mathrm{D}} \tag{15}$$

is the $M \times 1$ target slow-time vector at wrapped delay $\bar{\tau}$ corresponding to the g^{th} range interval, and

$$\mathbf{z}_{\mathrm{c},g}(\bar{\tau}) = \int \tilde{x}_{\mathrm{c},g}(\bar{\tau}, f_{\mathrm{D}})\mathbf{v}_g(f_{\mathrm{D}})df_{\mathrm{D}} \tag{16}$$

is the $M \times 1$ clutter slow-time vector for the g^{th} interval.

Assuming that the target motion relative to a range resolution bin is sufficiently small to prevent targets from traversing bins during a CPI, the processing of slow-time coded data operates entirely on $\mathbf{z}(\bar{\tau})$ from Equation (14) over all $\bar{\tau}$. The objective is to identify the moving targets within each $\tilde{x}_g(\bar{\tau}, f_{\mathrm{D}})$ for $g = 0, 1, \ldots, G-1$ by isolating the responses via distinct STC sequences for each range interval and associated slow-time processing. The scattering response can be determined via application of an interval-specific $M \times 1$ slow-time filter $\mathbf{w}_g(f_{\mathrm{D}})$ matched to Doppler f_{D}, which can be interpreted using Equation (14) as

$$\hat{\tilde{x}}_g(\bar{\tau}, f_{\mathrm{D}}) = \mathbf{w}_g^H(f_{\mathrm{D}})\mathbf{z}(\bar{\tau}), \tag{17}$$

where $(\bullet)^H$ is the Hermitian transpose. This separability of range intervals as a function of Doppler then sets the stage for subsequent separation of targets and clutter.

Using Equations (8), (14), and (17), the delay-Doppler response of a point target can be determined to evaluate the STC sequence's nominal ability to isolate range intervals. This point-target response (also known as the point spread function (PSF)), is typically defined for a matched response on receive. However, in the presence of STC, the definition of the PSF may be generalised to formulate the 'cross-PSF', which provides the expected response of a scatterer from the $\bar{g}^{\mathrm{th}}$ range interval folding into the g^{th} range interval as a function of delay and Doppler (for a theoretical zero-delay/zero-Doppler target). The maximum signal-to-noise ratio (SNR) Doppler filter (otherwise known as the Doppler matched filter) takes the form of the target response as

$$\mathbf{w}_{\mathrm{MF},g}(f_{\mathrm{D}}) = \frac{1}{M}\mathbf{v}_g(f_{\mathrm{D}}) = \frac{1}{M}\mathbf{v}(f_{\mathrm{D}}) \odot (\mathbf{T}_g\mathbf{d}(\theta)). \tag{18}$$

Therefore, assuming $\mathbf{w}_{\mathrm{MF},g}(f_{\mathrm{D}})$ is used as the processing method on receive, the cross-PSF for can be expressed as

$$\begin{aligned} \upsilon_{\bar{g},g}(\tau, f_{\mathrm{D}}) &= \frac{r(\tau)}{M}\mathbf{v}_g^H(f_{\mathrm{D}})\mathbf{v}_{\bar{g}}(0) \\ &= \frac{r(\tau)}{M}\mathbf{v}^H(f_{\mathrm{D}})((\mathbf{T}_g\mathbf{d}^*(\theta)) \odot (\mathbf{T}_{\bar{g}}\mathbf{d}(\theta))) \end{aligned} \tag{19}$$

for $\bar{g}, g = 0, 1, \ldots, G-1$, where $\mathbf{T}_{\bar{g}}\mathbf{d}(\theta) = \mathbf{v}_{\bar{g}}(0)$ is the slow-time response for a zero-Doppler target from the $\bar{g}^{\mathrm{th}}$ range interval, and

$$r(\tau) = \int_0^T s^*(t-\tau)s(t)dt \tag{20}$$

is the autocorrelation of pulsed waveform $s(t)$. The cross-PSF of Equation (19) can likewise be generalised to any different pair of values in $g = 0, 1, \ldots, G-1$. Note that the cross-PSF is separable in delay and Doppler; thus, the range disambiguation performance is minimally dependent on the underlying waveform modulation (i.e., largely dependent on STC sequence θ).

For example, consider a CPI of $M = 10^4$ LFM waveforms having time-bandwidth product $TB = 40$ (the same parameters used for the experimental demonstration in a later section) where the STC sequence is drawn from a uniform distribution on $[-\pi, \pi]$. Figure 2 shows Equation (19) for $\bar{g} = g = 0$ (Figure 2a) and $\bar{g} = 0$, $g = 1$ (Figure 2b). In the range-

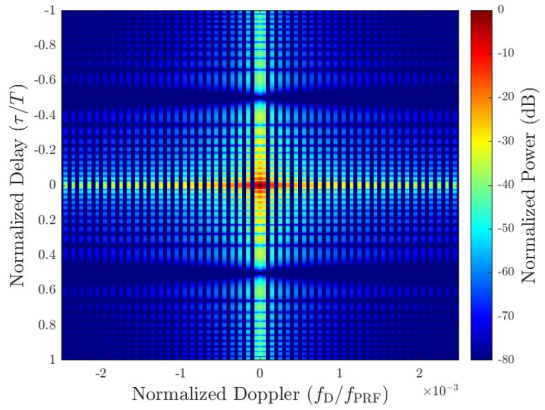

(a) PSF via (19) (in dB) for $\bar{g} = g = 0$, corresponding to the matched response in the $g = 0$ interval.

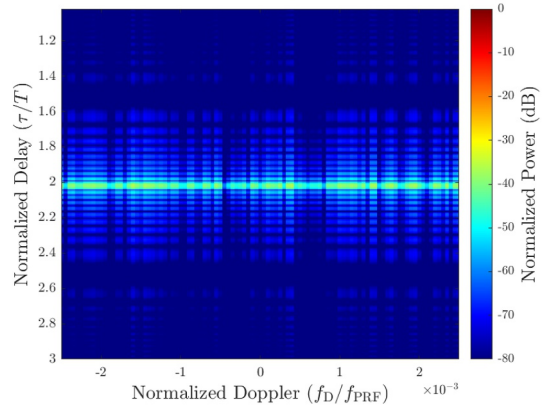

(b) Cross-PSF via (19) (in dB) for $\bar{g} = 0$, $g = 1$, corresponding to the folded response in the $g = 1$ interval.

FIGURE 2 | Expected delay/Doppler responses via the cross-PSF from Equation (19) (in dB) for unambiguous (top) and range-folded scattering (bottom). Both are zoomed in Doppler.

coincident (former) case, both range and Doppler compression are achieved since matched filters were used in both fast-time (pulse compression) and slow-time. In the range-folded (latter) case, range compression is achieved; however, the PSF is not compressed in Doppler due to a mismatch in the STC structure per Equation (19). Thus, energy is now spread across Doppler, which could obscure a lower-SNR target at the same range bin when folded.

Three methods are considered for their ability to isolate the desired scattering response:

1. Optimisation of the STC sequence θ_m to place nulls in desired Doppler regions of range-folded scattering to mitigate the cross-PSF Doppler sidelobes.
2. Max-SINR filtering (i.e., clutter cancelation) to null undesired scattering that would result in the largest cross-PSF Doppler responses.
3. Adaptive processing via the MR-RISR framework to mitigate cross-PSF Doppler sidelobes via adaptive estimation [27].

The following sections discuss and evaluate each of these approaches, and combinations thereof.

3.1 | Optimisation of STC Sequences

From Equation (19), it is apparent that the performance of range interval disambiguation is predominantly dependent[1] on $\mathbf{v}_g^H(f_D)\mathbf{v}_{\bar{g}}(0)$, which represents the Doppler response in the g^{th} range interval for a zero-Doppler point target in the $\bar{g}^{\text{th}}$ interval. With the knowledge that STC imparts separability of scattering from different range intervals, it is plausible that further suppression of certain range-folded responses could be achieved by applying an optimised STC sequence. Here, we generalise cross-PSF Doppler sidelobe minimisation via numerical optimisation techniques to mitigate the cross-responses for G intervals. While Doppler windowing can also be incorporated into the framework via a fixed (or optimised as in [7, 15]) taper, a rectangular Doppler window is assumed during optimisation, which is found to be amenable to tapering post-optimisation.

By collecting versions of Equation (10) according to some discretisation of Doppler into K bins prescribed by $f_{D,k}$, a Doppler steering matrix of dimension $M \times K$ can be formed as

$$\mathbf{V} = \left[\mathbf{v}(f_{D,0}), \mathbf{v}(f_{D,1}), \ldots, \mathbf{v}(f_{D,K-1})\right]. \tag{21}$$

Using Equation (19), the $K \times 1$ Doppler response at the g^{th} interval for a target in the $\bar{g}^{\text{th}}$ interval can then be expressed as

$$\boldsymbol{\upsilon}_{\bar{g},g} = \mathbf{V}^H\left(\left(\mathbf{T}_g\mathbf{d}^*(\theta)\right) \odot \left(\mathbf{T}_{\bar{g}}\mathbf{d}(\theta)\right)\right). \tag{22}$$

It is worth noting that the cross-PSF Doppler response cannot be explicitly characterised by mainlobe/sidelobe regions when $\bar{g} \neq g$ due to the mismatch of STC structures in the two range intervals. Rather, the cross-PSF energy of Equation (22) in Doppler is determined via the cross-correlation between the Doppler manifold for the g^{th} range interval and the zero-Doppler response for the $\bar{g}^{\text{th}}$ range interval. Thus, further suppression of range-folded scattering can be achieved within a specified Doppler span within Equation (22). The cost function used here is a modification of the generalised integrated sidelobe (GISL) metric [29] and can be stated as

$$J_{\bar{g},g} = \left\|\mathbf{e} \odot \boldsymbol{\upsilon}_{\bar{g},g}\right\|_p \tag{23}$$

for $2 \leq p < \infty$, where $\mathbf{e}$ is a selection vector comprised of ones and zeros to specify the Doppler span over which suppression is desired. Letting $p = 2$ allows Equation (23) to become an integrated Doppler sidelobe level (IDSL) metric, whereas $p \to \infty$ leads to a peak Doppler sidelobe level (PDSL) metric. Here, we use $p = 10$, which has been shown to be sufficiently large to achieve PDSL minimisation for practical waveform optimisation [29].

A generalised cost function subsuming the G range-folded intervals can subsequently be expressed as

$$J = \left(\sum_{b=1}^{G-1} \sum_{a=0}^{b-1} \left\| \mathbf{e} \odot \boldsymbol{\upsilon}_{a,b} \right\|_p^p \right)^{1/p} \tag{24}$$

By the conjugate-symmetry property of the Fourier transform, shaping $\boldsymbol{\upsilon}_{a,b}$ inherently shapes $\boldsymbol{\upsilon}_{b,a}$ as well. Therefore, it is sufficient for the double summation in Equation (24) to only include the $a < b$ terms, of which there are G-choose-2 combinations. The other implication of this property is that $\mathbf{e}$ must be symmetric about zero Doppler to achieve the same shaping of both $\boldsymbol{\upsilon}_{a,b}$ and $\boldsymbol{\upsilon}_{b,a}$. Alternative formulations of this cost function may leverage techniques such as Pareto weighting to prioritise minimisation for select (a, b) pairs. The gradient derivation of Equation (24) with respect to STC vector $\boldsymbol{\theta}$ is provided in Appendix A.

Regarding the Doppler selection vector $\mathbf{e}$, there are a variety of options to consider. First, setting $\mathbf{e} = \mathbf{1}$ (all ones) enables minimisation of Equation (24) at each Doppler within the entire unambiguous Doppler space, which eliminates spurious peaks that otherwise could produce false detections. Of course, this approach is limited by the available degrees-of-freedom, so it tends to yield a flattened response at a level near $-10\log_{10}M$ dB.

Another option sets $\mathbf{e}$ to ones only in a small span (denoted B_{notch}) centred around zero Doppler, with zeros elsewhere. Doing so places a broad notch around zero Doppler at the cost of pushing sidelobe energy to higher Doppler frequencies (as a result of conservation of ambiguity). Therefore, this approach is useful if the maximum unambiguous Doppler (here $\pm f_{\text{PRF}}/2$ for uniform PRIs) exceeds the anticipated span of Doppler shifts of illuminated targets.

To evaluate the relationship between notch width and achievable notch depth, multiple STC sequences were optimised by minimising Equation (24) for an $M = 100$ pulse CPI with $G = 2$ or $G = 3$ range intervals using various of notch widths for $\mathbf{e}$. For each notch width, 1000 Monte Carlo trials were conducted with randomly initialised STC sequences drawn from a uniform distribution over $[-\pi, \pi]$. A gradient-based optimisation was performed via the limited-memory Broyden-Fletcher-Goldfarb-Shanno (BFGS) algorithm [30], which is an unconstrained quasi-Newton method with per-iteration computation on the order of calculating the gradient. The particular implementation used here is the "minf_lbfgs" function from Tensorlab [31].

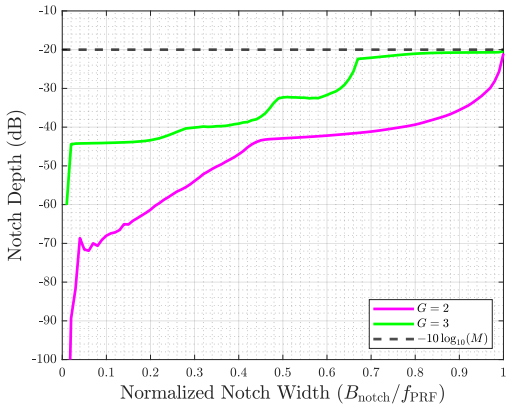

FIGURE 3 | Notch depth (in dB) as a function of relative notch width for optimised STC for $M = 100$ pulse CPI considering $G = 2$ (pink) and $G = 3$ (green) range intervals.

Figure 3 shows the average notch depth achieved as a function of notch width B_{notch} normalised by the PRF f_{PRF} (i.e., the full Doppler span). As B_{notch} increases, the achievable notch depth decreases due to the fixed number of degrees-of-freedom. For the $G = 2$ interval case (pink trace), the optimised notch depth outperforms the $-10\log_{10}M$ level one would expect from purely random instantiations for essentially all normalised notch widths. When an additional range interval is included for the $G = 3$ case (green trace), parity with the $-10\log_{10}M$ level is effectively reached at about 0.65 normalised notch width.

An alternative perspective is depicted in Figure 4, which illustrates the Doppler responses from Equation (22) for optimised STC sequences based on $G = 2$ (pink trace) and $G = 3$ (remaining traces), where $\mathbf{e}$ selects the zero-centred 20% of the Doppler space (indicated by the vertical dashed lines). It is clear that a deeper notch is attainable for the $G = 2$ case, in which a single pair of range-folded intervals must be addressed, as compared to the three pair-wise combinations for the $G = 3$ case.

3.2 | Maximum SINR Clutter Cancelation

In contrast to optimising STC, the distinct slow-time phase structure for each range interval can be leveraged in the context of clutter cancelation. Since clutter power is typically much higher than target responses, clutter suppression can greatly alleviate the Doppler sidelobe minimisation requirements of the cross-PSF. Using the target, clutter, and noise signal model from Equation (14), the maximum SINR filter can be employed. Assuming the target responses $\mathbf{z}_{\text{t},g}(\bar{\tau})$ are proportional to $\mathbf{v}_g(f_{\text{D}})$ from Equation (10), the slow-time filter that maximises the SINR for wrapped delay $\bar{\tau}$ of the g^{th} range interval and Doppler frequency f_{D} is known to be [32, 33]

$$\mathbf{w}_{\text{max-SINR},g}(\bar{\tau}, f_{\text{D}}) \propto \mathbf{R}_{\text{c+n}}^{-1}(\bar{\tau})\mathbf{v}_g(f_{\text{D}}), \tag{25}$$

where

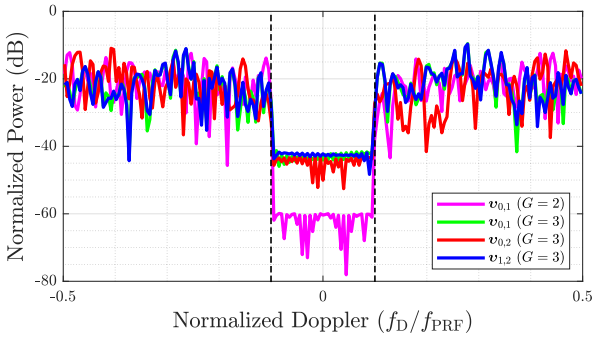

FIGURE 4 | Range-folded Doppler responses via cross-PSF Equation (22) (in dB) for $M = 100$ pulse CPI with normalised notch width $\frac{B_{\text{notch}}}{f_{\text{PRF}}} = 0.2$ (vertical dashed lines) and considering $G = 2$ (pink trace) and $G = 3$ (remaining traces) intervals.

$$\mathbf{R}_{\mathrm{c+n}}(\bar{\tau}) = \mathbb{E}\left[\left(\sum_{g=0}^{G-1} \mathbf{z}_{\mathrm{c},g}(\bar{\tau}) + \mathbf{u}(\bar{\tau})\right)\left(\sum_{g=0}^{G-1} \mathbf{z}_{\mathrm{c},g}(\bar{\tau}) + \mathbf{u}(\bar{\tau})\right)^{H}\right] \quad (26)$$

is the clutter + noise covariance matrix for wrapped delay $\bar{\tau}$ and $\mathbb{E}[\bullet]$ is the expectation operation.

Assuming that the clutter responses from the G intervals are mutually independent from one another and the noise process, Equation (26) can be expressed as

$$\mathbf{R}_{\mathrm{c+n}}(\bar{\tau}) = \sum_{g=0}^{G-1} \mathbf{R}_{\mathrm{c},g}(\bar{\tau}) + \mathbf{R}_{\mathrm{u}}. \quad (27)$$

Here, $\mathbf{R}_{\mathrm{u}} = \mathbb{E}\left[\mathbf{u}(\bar{\tau})\mathbf{u}^{H}(\bar{\tau})\right]$ is the noise covariance (assumed constant for all delay $\bar{\tau}$), and $\mathbf{R}_{\mathrm{c},g}(\bar{\tau}) = \mathbb{E}\left[\mathbf{z}_{\mathrm{c},g}(\bar{\tau})\mathbf{z}_{\mathrm{c},g}^{H}(\bar{\tau})\right]$ is the clutter covariance for the g^{th} range interval modified by the STC $\mathbf{d}(\theta)$ expressed as [12]

$$\mathbf{R}_{\mathrm{c},g}(\bar{\tau}) = \left(\mathbf{T}_g\mathbf{d}(\theta)\mathbf{d}^{H}(\theta)\mathbf{T}_g^{T}\right) \odot \mathbf{R}_{\mathrm{c}}(\bar{\tau} + gT_{\mathrm{p}}), \quad (28)$$

where $\mathbf{R}_{\mathrm{c}}(\tau)$ is the unmodifed clutter covariance versus true delay τ without STC. Based on the given assumptions regarding the structure and/or statistics of $\mathbf{R}_{\mathrm{c+n}}(\bar{\tau})$, there are many data-driven and model-driven techniques available in the literature with which to estimate Equation (27), to include (but not limited to) sample covariance matrix estimation [32, 34] and the Tyler M-estimator [35–37].

Assuming the noise covariance is white, zero-mean, complex-Gaussian noise with variance σ_{u}^2 (i.e., $\mathbf{R}_{\mathrm{u}} = \sigma_{\mathrm{u}}^2\mathbf{I}_{M\times M}$), the max-SINR filters can be normalised to prevent scaling of the noise subspace as

$$\mathbf{w}_{\text{max-SINR},g}(\bar{\tau}, f_{\mathrm{D}}) = \frac{\sigma_{\mathrm{u}}^2}{M}\mathbf{R}_{\mathrm{c+n}}^{-1}(\bar{\tau})\mathbf{v}_g(f_{\mathrm{D}}). \quad (29)$$

Applying these filters to the pulse-compressed received data $\mathbf{z}(\bar{\tau})$ (as in Equation (17)) cancels the clutter of each range interval, thus mitigating Doppler sidelobes induced by clutter. Per Equation (28), the STC imparts a unique phase structure to the clutter responses from each range interval. If the clutter subspaces of $\mathbf{R}_{\mathrm{c}}(\bar{\tau} + gT_{\mathrm{p}})$ for $g = 0, 1, ..., G-1$ are similar, STC effectively decorrelates the G clutter responses, enabling each region to be uniquely nulled based on its corresponding clutter subspace. Because of this decorrelation, the rank of the overall clutter subspace of $\mathbf{R}_{\mathrm{c+n}}(\bar{\tau})$ can be expected to be G times greater than for any individual range interval. Therefore, this range disambiguation technique is only feasible as long as the collective clutter rank from all G intervals is less than the slow-time dimensionality (i.e., number of pulses).

3.3 | Multi-Range RISR (MR-RISR)

Recently introduced in [27], cross-PSF sidelobe energy can also be addressed by adaptive Doppler processing. Specifically, the Doppler processing version [38] of the reiterative super-resolution algorithm [20], itself an extension of reiterative minimum mean-square error (RMMSE) estimation [24, 39], was extended to model scattering arriving from multiple range intervals having STC, and thus denoted as multi-range RISR or MR-RISR (see [9, 10] for other STC-based adaptive methods). This approach leverages a structured signal model for the snapshot data vector $\mathbf{z}(\bar{\tau})$ from Equation (14) to adaptively estimate the Doppler spectrum for each wrapped delay bin $\bar{\tau}$ and range interval g. Doing so has two clear advantages when compared to the max-SINR processing discussed in Section III-B, namely: (1) the estimated Doppler spectrum exhibits super-resolution that can facilitate discrimination of closely-spaced scatterers in Doppler, and (2) statistical knowledge of the clutter covariance $\mathbf{R}_{\mathrm{c+n}}(\bar{\tau})$ is not required, thus mitigating issues arising from training data heterogeneity and sample support.

To enable adaptive estimation of the scattering across range and Doppler (over multiple range intervals), the slow-time $\mathbf{z}(\bar{\tau})$ is modelled via

$$\begin{aligned}\mathbf{z}(\bar{\tau}) &= \sum_{g=0}^{G-1}\left(\mathbf{T}_g\mathbf{d}(\theta)\right) \odot \left(\mathbf{V}\mathbf{x}_g(\bar{\tau})\right) + \mathbf{u}(\bar{\tau}) \\ &= \sum_{g=0}^{G-1}\mathbf{V}_g\mathbf{x}_g(\bar{\tau}) + \mathbf{u}(\bar{\tau}),\end{aligned} \quad (30)$$

where

$$\mathbf{V}_g = \left[\mathbf{v}_g(f_{\mathrm{D},0}), \mathbf{v}_g(f_{\mathrm{D},1}), ..., \mathbf{v}_g(f_{\mathrm{D},K-1})\right] \quad (31)$$

is the $M \times K$ Doppler matrix for the g^{th} range interval, and

$$\mathbf{x}_g(\bar{\tau}) = \left[x_g(\bar{\tau}, f_{\mathrm{D},0}), x_g(\bar{\tau}, f_{\mathrm{D},1}), ..., x_g(\bar{\tau}, f_{\mathrm{D},K-1})\right]^{T} \quad (32)$$

is the $K \times 1$ parameter vector representing the scattering across Doppler at wrapped delay $\bar{\tau}$ for the g^{th} range interval.

Imposing a gain-constrained form has been found to improve robustness of the spectral estimate [21]; thus, the optimisation problem to determine the MR-RISR filter $\mathbf{w}_g(\bar{\tau}, f_{\mathrm{D},k})$ is expressed as

$$\begin{aligned}\underset{\mathbf{w}_g(\bar{\tau}, f_{\mathrm{D},k})}{\text{minimize}} \quad & \mathbb{E}\left[\left|x_g(\bar{\tau}, f_{\mathrm{D},k}) - \mathbf{w}_g^{H}(\bar{\tau}, f_{\mathrm{D},k})\mathbf{z}(\bar{\tau})\right|^2\right] \\ \text{s.t.} \quad & \mathbf{w}_g^{H}(\bar{\tau}, f_{\mathrm{D},k})\mathbf{v}_g(f_{\mathrm{D},k}) = 1.\end{aligned} \quad (33)$$

The resulting filter takes the form [21]

$$\mathbf{w}_{\text{MR-RISR},g}(\bar{\tau}, f_{\mathrm{D},k}) = \frac{\mathbf{R}^{-1}(\bar{\tau})\mathbf{v}_g(f_{\mathrm{D},k})}{\mathbf{v}_g^{H}(f_{\mathrm{D},k})\mathbf{R}^{-1}(\bar{\tau})\mathbf{v}_g(f_{\mathrm{D},k})}, \quad (34)$$

where

$$\mathbf{R}(\bar{\tau}) = \sum_{g=0}^{G-1}\mathbf{V}_g\mathbf{P}_g(\bar{\tau})\mathbf{V}_g^{H} + \mathbf{R}_{\mathrm{u}} \quad (35)$$

is a structured data covariance matrix comprising the G range-folded intervals, and $\mathbf{P}_g(\bar{\tau})$ is a $K \times K$ diagonal matrix, the diagonal elements of which are

$$\left[\mathbf{P}_g(\bar{\tau})\right]_{kk} = \mathbb{E}\left[|x_g(\bar{\tau}, f_{\mathrm{D},k})|^2\right], \tag{36}$$

that correspond to the expected scattering variance at the k^{th} Doppler in the g^{th} range interval at wrapped delay $\bar{\tau}$. A derivation of Equation (34) can be found in Appendix B. Within the RMMSE framework, the statistical representation of $\mathbf{P}_g(\bar{\tau})$ is replaced by a deterministic expression by approximating it with the magnitude-square of the current Doppler spectrum estimate, that is, $\mathbb{E}\left[|x_g(\bar{\tau}, f_{\mathrm{D},k})|^2\right] \approx |\hat{x}_g(\bar{\tau}, f_{\mathrm{D},k})|^2$. Therefore, the MR-RISR algorithm becomes iterative via recalculation of Equation (34) when provided with new Doppler estimates via $\hat{x}_g(\bar{\tau}, f_{\mathrm{D},k}) = \mathbf{w}^H_{\mathrm{MR\text{-}RISR},g}(\bar{\tau}, f_{\mathrm{D},k})\mathbf{z}(\bar{\tau})$. It has been found that 5–10 iterations are typically required for convergence.

Note that MR-RISR does not explicitly separate desired scattering (i.e., targets) from undesired scattering (i.e., clutter). Instead, this method aims to improve the estimate of all scattering. By doing so, the algorithm naturally suppresses interfering sidelobe energy that would otherwise be present. However, it should be noted that MR-RISR relies on a discretisation of the continuous Doppler space, meaning that model mismatch can limit the sidelobe suppress in extreme scenarios—such as when the discretisation is too coarse (i.e., $K \approx M$) and the clutter-to-noise ratio is large (e.g., 80 dB). While not discussed further here, methods have been developed to account for this model mismatch in the case that the clutter + noise covariance $\mathbf{R}_{\mathrm{c+n}}(\bar{\tau})$ is known or estimated [40].

The matrix inversion of $\mathbf{R}(\bar{\tau})$ costs $O(M^3)$ for each iteration and each wrapped delay bin, though parallelisable over delay. The multiplication $\mathbf{v}_g^H(f_{\mathrm{D},k})\mathbf{R}^{-1}(\bar{\tau})\mathbf{v}_g(f_{\mathrm{D},k})$ costs $O(M^2)$ and is performed KG times. For I iterations, the total cost is $O((M^3 + M^2KG)I)$, though the latter multiplication is also parallelisable.

4 | SINR Analysis of Range Disambiguation

Consider the signal model from Equation (14) for a single target in zero-mean clutter + noise having covariance $\mathbf{R}_{\mathrm{c+n}}(\bar{\tau})$. Let the target response be $\mathbf{z}_{\mathrm{t},g}(\bar{\tau}_0) = \gamma\mathbf{v}_g(f_{\mathrm{D}})$ at range interval g and wrapped delay $\bar{\tau}_0$. The output SINR after application of filter $\mathbf{w}_g(\bar{\tau}, f_{\mathrm{D}})$ to data vector $\mathbf{z}(\bar{\tau})$ can be expressed as [32].

$$\mathrm{SINR}(\mathbf{w}_g(f_{\mathrm{D}})) = \frac{|\gamma|^2|\mathbf{w}_g^H(f_{\mathrm{D}})\mathbf{v}_g(f_{\mathrm{D}})|^2}{\mathbf{w}_g^H(f_{\mathrm{D}})\mathbf{R}_{\mathrm{c+n}}\mathbf{w}_g(f_{\mathrm{D}})}, \tag{37}$$

where dependence on $\bar{\tau}_0$ is excluded for brevity. The Doppler filter can be any of Equations (18) and (29), or Equation (34). Subsequently, SINR loss is calculated by normalising Equation (37) with the optimal output SNR (i.e., when no clutter is present and the optimal filter is applied) [32]. Assuming a white noise covariance (i.e., $\mathbf{R}_{\mathrm{u}} = \sigma_{\mathrm{u}}^2\mathbf{I}_{M\times M}$), the optimal output SNR is $\frac{M|\gamma|^2}{\sigma_{\mathrm{u}}^2}$, and the SINR loss can therefore be expressed as

$$L_{\mathrm{SINR}}(\mathbf{w}_g(f_{\mathrm{D}})) = \frac{\sigma_{\mathrm{u}}^2}{M}\frac{|\mathbf{w}_g^H(f_{\mathrm{D}})\mathbf{v}_g(f_{\mathrm{D}})|^2}{\mathbf{w}_g^H(f_{\mathrm{D}})\mathbf{R}_{\mathrm{c+n}}\mathbf{w}_g(f_{\mathrm{D}})}, \tag{38}$$

which removes the dependence on target scaling γ. The SINR loss in Equation (38) allows direct comparison between the different STC range disambiguation methods.

Consider $M = 100$ pulses in the CPI and $G = 2$ range intervals to disambiguate, for a total of $M + G - 1 = 101$ total pulses when accounting for fill pulses. Two STC sequences are evaluated: (1) a random STC sequence where each phase is drawn from a uniform random distribution on $[-\pi, \pi]$, and (2) an optimised STC using the method discussed in Section 3.1 having normalised notch width $\frac{B_{\mathrm{notch}}}{f_{\mathrm{PRF}}} = 0.6$ and using $p = 10$ in Equation (24). Along with the previously discussed Doppler filters (i.e., Equations (18) and (29), or Equation (34)), an additional tapered MF case is included, which is expressed as

$$\mathbf{w}_{\mathrm{T\text{-}MF},g}(f_{\mathrm{D}}) = \frac{1}{M}\mathbf{t} \odot \mathbf{v}_g(f_{\mathrm{D}}), \tag{39}$$

where $\mathbf{t}$ is an $M \times 1$ slow-time taper normalised to have unit white noise gain via $\mathbf{t}^H\mathbf{t} = 1$. Note that the STC optimisation routine in Section 3.1 effectively ignores tapering (via use of rectangular taper), though other tapers can easily be incorporated with minor modifications (see [15] for joint STC and taper design). Here, a 60 dB Taylor window is chosen to show that tapering can still be applied to these optimised STCs and thus achieve improved performance, though additional performance improvement may potentially be attained by including the desired taper in the optimisation process. This Taylor window results in a 1.89 dB SNR loss.

Figure 5 shows the cross-PSF Doppler responses using $K = 4M$ Doppler points (i.e., over-sampled by 4) for the random and optimised STC sequences using rectangular and Taylor tapering, where the cross-PSF expression from Equation (22) has been generalised to include Doppler tapering as

$$\boldsymbol{\upsilon}_{\bar{g},g} = \mathbf{V}^H\left(\mathbf{t} \odot \left(\mathbf{T}_g\mathbf{d}^*(\theta)\right) \odot \left(\mathbf{T}_{\bar{g}}\mathbf{d}(\theta)\right)\right). \tag{40}$$

The optimised STC with no taper (red trace) achieves approximately 20 dB of additional sidelobe suppression (to about −40 dB) relative to the randomised code, which agrees with

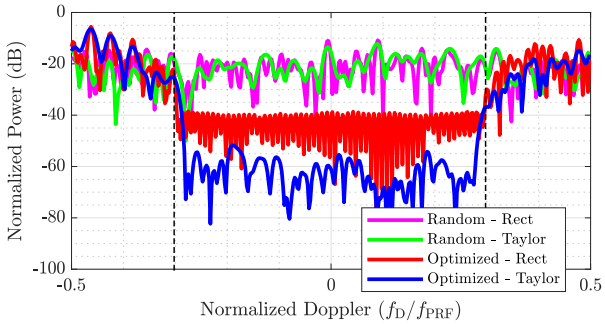

FIGURE 5 | Range-folded Doppler responses via cross-PSF cut $\boldsymbol{\upsilon}_{0,1}$ from Equation (22) (in dB) for $M = 100$ pulse CPI and $G = 2$ range intervals for random STC with no taper (pink), random STC with Taylor taper (green), optimised STC with no taper (red), and optimised STC with Taylor taper (blue). Notch bandwidth of $\frac{B_{\mathrm{notch}}}{f_{\mathrm{PRF}}} = 0.6$ indicated by vertical dashed lines.

Figure 3 since the random code will have an average sidelobe level of approximately $-10\log_{10}M = -20$ dB. After applying the Taylor window, the sidelobes for random STC stay at the same level, while optimised STC yields roughly another 10 dB reduction, thereby demonstrating that combining tapering with STC optimisation can improve range disambiguation even when tapering in not included in the design.

Using these random and optimised STC sequences, the analytical SINR performance is evaluated via the SINR loss from Equation (38) using the untapered/tapered matched filters from Equations (18) and (39). The clutter power spectral density for each of the $G = 2$ range intervals is assumed flat over a normalised Doppler width Δ_g centred about 0 Hz. The $(m, m')^{\text{th}}$ index of the resulting clutter covariances at wrapped delay $\overline{\tau}_0$ for intervals $g = 0, 1$ can be expressed as

$$\left[\mathbf{R}_{\text{c}}(\overline{\tau}_0 + gT_{\text{p}})\right]_{mm'} = \sigma^2_{\text{c},g}\,\text{sinc}\big(\pi\Delta_g(m - m')\big), \tag{41}$$

where $\sigma^2_{\text{c},g}$ is the clutter power for the g^{th} interval. For this analysis, let $\sigma^2_{\text{c},0} = 10^4$ and $\sigma^2_{\text{c},1} = 10^3$ to account for some loss as a function of range interval, and let $\Delta_0 = \Delta_1 = 0.05$. The overall clutter covariance $\mathbf{R}_{\text{c},g}(\overline{\tau}_0)$ for each STC is then obtained using Equation (28), with the clutter + noise covariance $\mathbf{R}_{\text{c+n}}(\overline{\tau}_0)$ determined via Equation (27) for white noise covariance $\mathbf{R}_{\text{u}} = \sigma^2_{\text{u}}\mathbf{I}_{M\times M}$ having unit variance $\sigma^2_{\text{u}} = 1$. To establish a performance bound, the SINR loss from Equation (38) is also evaluated for the max-SINR case from Equation (29) under the assumption of clairvoyant clutter + noise covariance knowledge.

Figure 6 shows the SINR losses for these various cases when the filter is aligned to the $g = 0$ (Figure 6a) and $g = 1$ intervals (Figure 6b). In Figure 6a, the clutter for the $g = 1$ interval folds into the $g = 0$ interval. Consequently, the random STC exhibits significant loss for both untapered and tapered filters. Figure 6b has similar behaviour, albeit with 10 dB worse SINR loss for random STC due to the higher power clutter from the $g = 0$ interval. After optimisation, the notched region demonstrates improved SINR performance for both range intervals. The untapered matched filter cases (in red) have modest improvement due to sinc-like clutter sidelobes that are coincident with the target (i.e., not folded). The Taylor window further improves SINR performance due to suppression of both the range-folded and range-coincident clutter sidelobes (inclusive of taper loss). The width of the improved SINR loss region for the optimised/Taylor case is slightly less than the optimised width of $\frac{B_{\text{notch}}}{f_{\text{PRF}}} = 0.6$ (vertical dashed lines) due to the narrow width $\Delta_g = 0.05$. Therefore, the total width of the SINR loss improvement region is approximately $0.6 - 0.05 = 0.55$ in normalised Doppler.

The black and grey traces in Figure 6 represent the optimal SINR loss curves for the random and optimised STC sequences, respectively, using max-SINR filtering from Equation (29) with clairvoyant $\mathbf{R}_{\text{c+n}}(\overline{\tau}_0)$. While both STC sequences exhibit excellent performance, STC optimisation does have an effect on SINR loss. The random STC sequence (black trace) has a roughly flat SINR loss outside of the clutter region, varying between -1.0 and -0.5 dB. The optimised STC (grey trace) exhibits nearly 0 dB SINR loss within the Doppler notched region of $\frac{f_{\text{D}}}{f_{\text{PRF}}} = \pm 0.3$ and outside the clutter region, but degrades somewhat (up to -3.3 dB) at higher Doppler since the optimisation has pushed sidelobe energy into these regions.

Now consider MR-RISR processing via Equation (38) for $K = 4M = 400$ over-sampled Doppler bins and $G = 2$ range intervals. Because MR-RISR determines filters iteratively for a single snapshot of data, the SINR loss is evaluated over 100 trials for each frequency $f_{\text{D},k}$ with different independent instantiations of target, clutter, and noise using the same random/optimised STC sequences as above. The clutter + noise process is drawn from a zero-mean complex Gaussian distribution with covariance $\mathbf{R}_{\text{c+n}}(\overline{\tau}_0)$ using the clutter and noise covariances described previously, and a target response of $\mathbf{z}_{\text{t},g}(\overline{\tau_0}) = \gamma\mathbf{v}_g(f_{\text{D},k})$ is injected with $\gamma = 10e^{j\phi}$, where phase ϕ is randomised for every trial.

Figure 7 shows SINR loss for the random and optimised STC sequences using MR-RISR and clairvoyant max-SINR filtering when matched to the $g = 0$ (Figure 7a) and $g = 1$ intervals (Figure 7b). The SINR loss for each range interval approximately mirror one another due to the conjugate-symmetry of the range-folded clutter. Outside of the clutter region, MR-RISR achieves 2 - 3 dB more SINR loss (on average) compared to clairvoyant max-SINR with modest improvement for optimised STC within the designed notch interval of +/−0.3 (vertical dashed lines) and modest degradation outside this interval. It should be emphasised that MR-RISR achieves this (average) performance with no knowledge of the clutter + noise covariance.

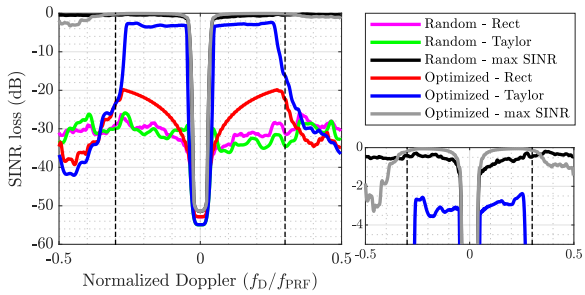

(a) SINR losses (in dB) for the $g = 0$ range interval.

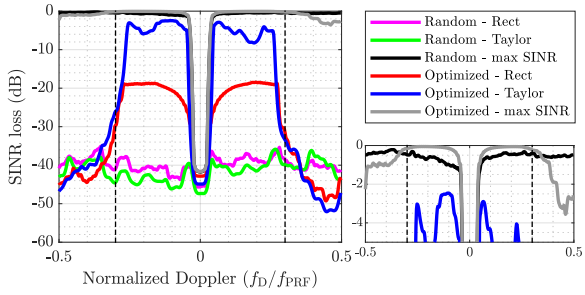

(b) SINR losses (in dB) for the $g = 1$ range interval.

FIGURE 6 | SINR losses (in dB) from Equation (38) for random and optimised STC sequences without tapering Equation (18), Taylor tapering Equation (39), and max-SINR filtering from Equation (29) for $M = 100$ pulse CPI and $G = 2$ range intervals. Notch bandwidth of $\frac{B_{\text{notch}}}{f_{\text{PRF}}} = 0.6$ indicated by vertical dashed lines.

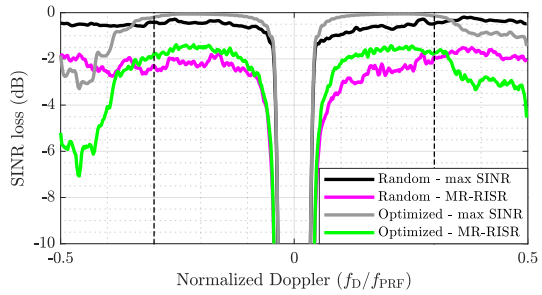

(a) SINR losses (in dB) for the $g = 0$ range interval.

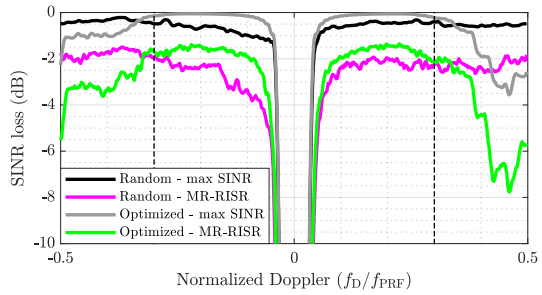

(b) SINR losses (in dB) for the $g = 1$ range interval.

FIGURE 7 | SINR losses from Equation (38) (in dB) for random and optimised STC sequences using max-SINR filtering from Equation (29) and MR-RISR from Equation (34) (100 trials averaged) with $K = 400$ over-sampled frequency bins and 10 iterations for $M = 100$ pulse CPI and $G = 2$ range intervals. Notch bandwidth of $\frac{B_{\text{notch}}}{f_{\text{PRF}}} = 0.6$ indicated by vertical dashed lines.

5 | Open-Air Experimental Evaluation of Range Disambiguation Methods

Open-air measurements are used to experimentally assess the range disambiguation performance for the techniques discussed in Section 3. Here, we illuminate $G = 2$ range intervals using $T_p = 3$ μs and $M = 10^4$ pulses (for a CPI of 3 ms). The short PRI and large number of pulses is necessary to induce range-ambiguous scattering while maintaining sufficient Doppler resolution and energy-on-target to accommodate the hardware constraints of low-power transmission. From the roof of a building at the University of Kansas, the roads near the west entrance to campus (in the first range interval) and the 23rd & Iowa St. intersection (in the second range interval) are illuminated using an S-band dish antenna. Figure 8 shows the field of regard with iso-range lines labelled, where the regions between adjacent red and blue circles (0–150, 300–450, 450–600, 750–900 m) are partially eclipsed, and the regions between blue circles (150–300, 600–750 m) correspond to non-blind, non-eclipsed ranges. The red circles at 450 and 900 m represent the end ranges of the first and second range intervals, respectively. A list of the test equipment is provided in Table 1, and a block diagram of the entire system is shown in Figure 9. Due to the low-power transmission, the radar testbed was operated in a simultaneous transmit and receive mode.

A total of five transmission cases are evaluated (with and without STC), with each case transmitting LFM waveforms having a 40 MHz swept bandwidth and $T = 1$ μs pulse duration.[2] Transmission Case 1 does not employ STC, but instead

FIGURE 8 | Overhead view of the field of regard for demonstration of range disambiguation using STC.

TABLE 1 | Equipment used for experimental demonstration.

Device	Manufacturer	Model number
SDR	Per Vices	Cyan 2r2t
RF PA	Maury Microwave	MPA-2G-18G-20
RF LNA	Mini-Circuits	ZX60-04183LN+
S-band BPF	Mini-Circuits	VBFZ-3590-S+
Antennas	—	S-band dish
1st LO RF Gen	Rohde & Schwarz	SMA-100B

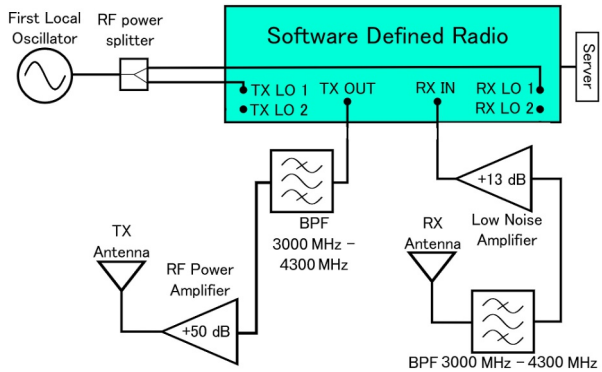

FIGURE 9 | Block diagram of radar testbed used for experimental demonstration.

uses a longer PRI ($T_p = 9$ μs) with the same number of pulses (i.e., same energy-on-target) to establish 'ground truth' scattering from both range intervals. Case 2 likewise does not employ STC and uses the shorter PRI ($T_p = 3$ μs), thus experiences range-folding. Case 3 applies a uniformly-random (unoptimised) STC sequence to the shorter PRI.

The remaining two cases possess STC sequences optimised via Equation (24) for $G = 2$ intervals. Case 4 employs optimised

STC with a notch width spanning the entire unambiguous Doppler space, that is, $\frac{B_{\text{notch}}}{f_{\text{PRF}}} = 1$. Alternatively, Case 5 applies optimised STC with a notch width covering 10% of the Doppler space centred around zero, that is, $\frac{B_{\text{notch}}}{f_{\text{PRF}}} = 0.1$, which corresponds to the velocity span of $|v| < 734.7854$ m/s. Table 2 summarises the five transmission cases, which were emitted sequentially to approximately illuminate the same scene.

Figure 10 shows the range-folded Doppler responses via cross-PSF $\boldsymbol{\upsilon}_{1,0}$ from Equation (22). Figure 10a represents the unoptimised STC sequence used in Case 3. Figure 10b represents the optimised STC sequence used in Case 4, which offers a PDSL improvement of ∼9.2 dB over Case 3, albeit with the same IDSL. Finally, Figure 10c represents the optimised STC sequence used in Case 5, which boasts an additional ∼50 dB of suppression over Case 3 within $\left|\frac{f_{\text{D}}}{f_{\text{PRF}}}\right| < 0.05$. Despite the fact that $\frac{f_{\text{D}}}{f_{\text{PRF}}} = \pm 0.05$ well exceeds the expected span of clutter/mover Doppler shifts for this test setup, further decreasing the notch depth by narrowing the notch width yields no meaningful benefit for the modest expected clutter-to-noise ratio of this experiment.

TABLE 2 | Summary of test cases.

Case 1	No STC, $T_{\text{p}} = 9$ μs
Case 2	No STC, $T_{\text{p}} = 3$ μs
Case 3	Uniform random (unoptimised) STC, $T_{\text{p}} = 3$ μs
Case 4	Optimised STC (100% notch), $T_{\text{p}} = 3$ μs
Case 5	Optimised STC (10% notch), $T_{\text{p}} = 3$ μs

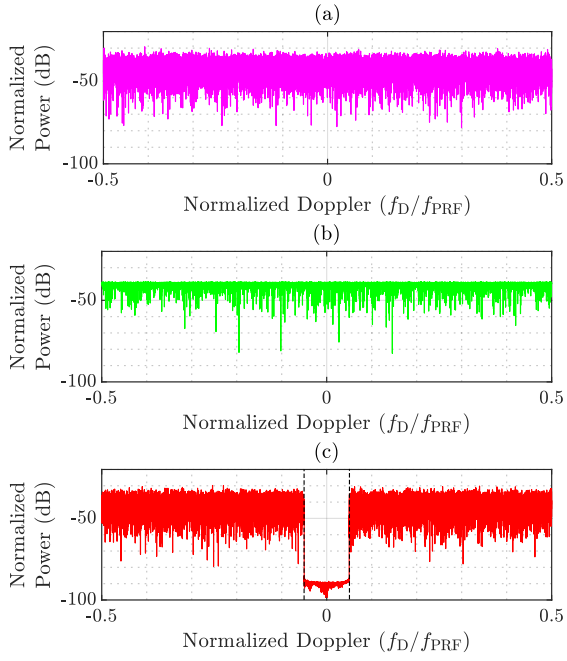

FIGURE 10 | Range-folded Doppler responses via cross-PSF cut $\boldsymbol{\upsilon}_{1,0}$ from Equation (22) (in dB) for a CPI of $M = 10^4$ pulses and $G = 2$ range intervals for: (a) Case 3—random STC, (b) Case 4—optimised STC w/100% notch, and (c) Case 5—optimised STC w/10% notch indicated by vertical dashed lines.

Cases 2–5 are processed using the three methods of Taylor-tapered matched filtering from Equation (39), max-SINR filtering from Equation (29), and MR-RISR from Equation (34). Case 1 is processed using Taylor-tapered matched filtering and serves as a 'ground truth.' Rather than data-driven adaptation, the clutter + noise covariance is deterministically constructed using Equations (27) and (28) with covariance matrix $\mathbf{R}_{\text{c}}(\tau)$ taking the form of a Gaussian power spectral density as

$$[\mathbf{R}_{\text{c}}(\tau)]_{mm'} = \sigma_{\text{c}}^2 \, e^{-0.5(2\pi\Delta(m-m'))^2}. \tag{42}$$

The noise power is set to $\sigma_{\text{u}}^2 = -12$ dB, the clutter power is set to $\sigma_{\text{c}}^2 = 80$ dB, and the clutter width is set to $\Delta = M \times 10^{-6}$, which was found to work well for this dataset. Because the experiment involves a stationary platform, the majority of scattering resides around zero Doppler; thus, the clutter spectrum can be easily predicted.[3] Note that the clutter covariance $\mathbf{R}_{\text{c}}(\tau)$ is set to be equal over all delay τ, which results in over-suppression of the clutter at some ranges. This deterministic approximation is sufficient to illustrate the properties of the max-SINR filter for this open-air data collect. Finally, the MR-RISR routine [4] is applied using $K = 5M$ over-sampled frequency bins and is terminated after five iterations.

Figure 11 shows the estimated range-Doppler map (RDM) (in dB) for Case 1 where no STC is applied and the extended PRI avoids range-folding. The Taylor taper significantly suppresses clutter sidelobes at the cost of degraded Doppler resolution, though it is still 3× finer than Cases 2–5. Multiple movers are clearly visible over the 0–900 m range interval, which corresponds to $G = 2$ folded range intervals for Cases 2–5. The zoomed-in right-hand panel of Figure 11 shows multiple movers (cars/trucks) between 270 and 350 m, which will serve as a useful 'region-of-interest' comparison for Cases 2–5.

Figure 12 shows the estimated RDMs (in dB) for Case 2, which has no STC, and the PRI is reduced to $T_{\text{p}} = 3$ μs to induce range-

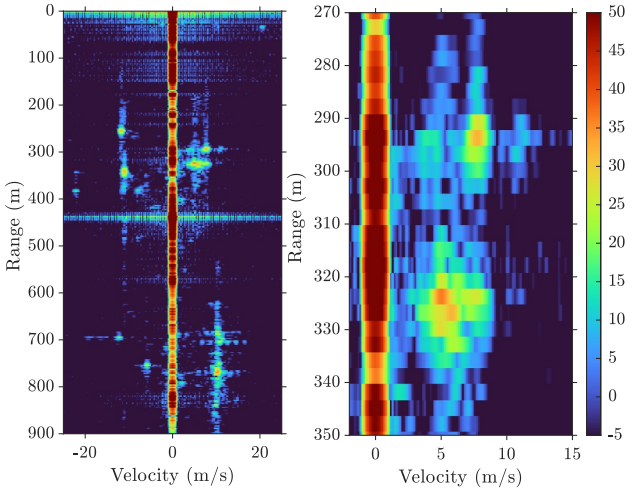

FIGURE 11 | Case 1—Open-air range-Doppler estimates (in dB) using no STC and $T_{\text{p}} = 9$ μs. Receive processed with a Taylor-tapered matched filter. Zoomed-in response on right.

folding. Figure 12a is the RDM for Taylor-tapered matched filtering, Figure 12b uses max-SINR filtering, and Figure 12c is the MR-RISR result. Zoomed-in responses for the region-of-interest are shown beneath each RDM. Note that the $g = 0$ range interval (i.e., 0–450 m) is replicated for the $g = 1$ range interval (450–900 m). Therefore, movers from the $g = 1$ and $g = 0$ intervals are folded onto each other and cannot be distinguished. Range-folding aside, max-SINR processing removes the clutter (both coincident and folded), leaving only movers (albeit range ambiguous). The mover responses for max-SINR filtering avoid the resolution degradation of Taylor tapering, while MR-RISR goes further to realise a degree of Doppler super-resolution. The former also exhibits Doppler sidelobes from the larger mover responses that are suppressed by the latter. However, due to the lack of STC, range disambiguation is achieved by neither approach. Case 2 therefore serves as the 'worst-case' scenario.

The RDMs for Case 3 (random STC) are shown in Figure 13 for Taylor-taper matched filtering (Figure 13a), max-SINR filtering (Figure 13b), and MR-RISR processing (Figure 13c). The region-of-interest responses are again found beneath each RDM which, when compared to Figure 11, demonstrate the disambiguation of the $g = 0$ and $g = 1$ range intervals with varying degrees of success. The Taylor-tapered matched filtering exhibits high cross-PSF Doppler sidelobes from folded clutter, due to the taper's inability to reduce the cross-PSF Doppler sidelobes for a random STC—as predicted in Figure 6. However, the max-SINR and MR-RISR estimates exhibit excellent isolation of the folded range intervals. Similar to Figure 12, max-SINR filtering suppresses clutter but preserves Doppler sidelobes from movers, which are suppressed by MR-RISR along with some Doppler super-resolution.

Figure 14 then displays the RDM estimates for Case 4, where the STC sequence is optimised to reduce sidelobes over 100% of the Doppler space. While the PDSL for Case 4 is improved by approximately 9.2 dB over Case 3, the IDSL is the same. As a

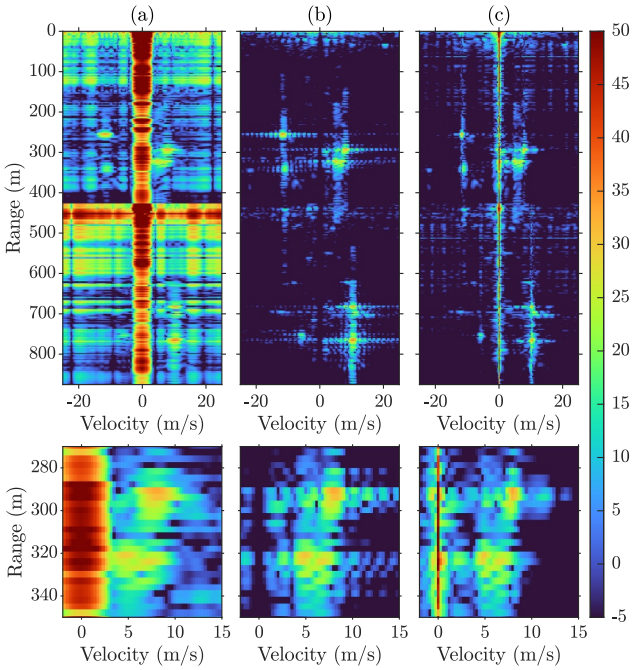

FIGURE 13 | Case 3—Open-air range-Doppler estimates (in dB) using random STC on transmit and $T_p = 3$ μs: (a) Taylor-taper matched filtering, (b) max-SINR filtering, and (c) MR-RISR ($K = 5M$ and five iterations). Zoomed-in responses below each figure.

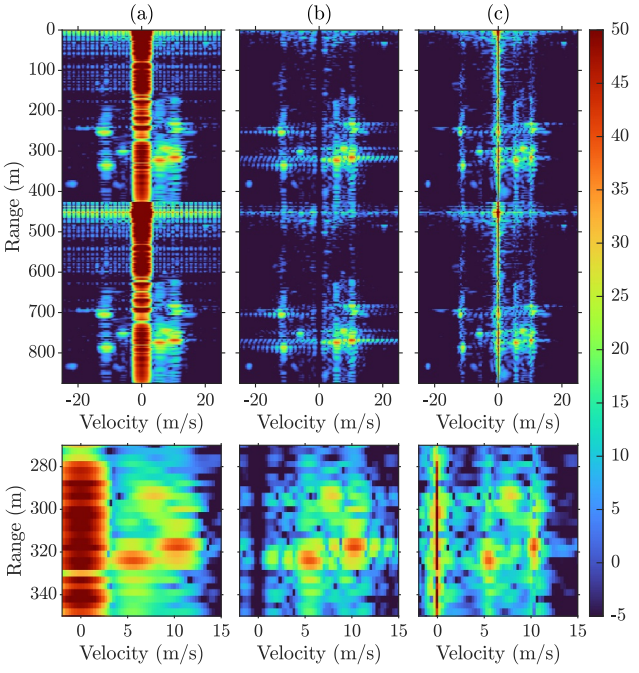

FIGURE 12 | Case 2—Open-air range-Doppler estimates (in dB) using no STC for $T_p = 3$ μs: (a) Taylor-taper matched filtering, (b) max-SINR filtering, and (c) MR-RISR ($K = 5M$ and five iterations). Zoomed-in responses below each figure.

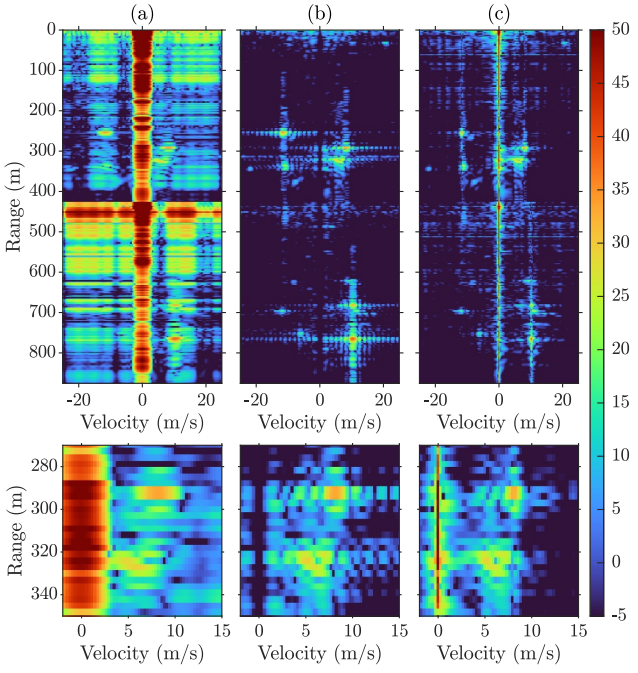

FIGURE 14 | Case 4—Open-air range-Doppler estimates (in dB) using optimised STC (100%) on transmit and $T_p = 3$ μs: (a) Taylor-taper matched filtering, (b) max-SINR filtering, and (c) MR-RISR ($K = 5M$ and 5 iterations). Zoomed-in responses below each figure.

result, the RDM responses in Figures 13 and 14 are qualitatively identical for each processing method.

Figure 15 shows the estimated RDMs for the Case 5 transmission scenario where the STC sequence is optimised to reduce the folded cross-PSF sidelobes in the centre 10% of the Doppler space, with Taylor-tapered matched filtering in Figure 15a, max-SINR filtering in Figure 15b, and MR-RISR in Figure 15c, with the region-of-interest responses beneath each. The max-SINR and MR-RISR RDMs do not exhibit much qualitative improvement over Cases 3 and 4, though as was shown in Section 4, the SINR loss for max-SINR and MR-RISR is improved for an optimised STC relative to a random STC. The most obvious improvement can be found in Figure 15a (tapered matched filtering), where the cross-PSF sidelobes have been suppressed via STC optimisation, yielding a reduced background floor. This suppression of cross-PSF sidelobe energy can be best demonstrated by observing the 450 m cuts of Figures 13a, 14a, and 15a, which have been collected in Figure 16. Case 5 exhibits a near 50 dB mitigation of folded cross-PSF sidelobes that are present for Cases 3 and 4. Note that this behaviour is only possible because the scattering is contained within a Doppler interval that is much less than the unambiguous Doppler space.

Finally, to illustrate a comparison of range disambiguation across the different methods, Figure 17 shows the RDM cut at 318 m for (a) Case 2, (b) Case 3, (c) Case 4, and (d) Case 5 for Taylor-tapered matched filtering (pink), max-SINR filtering (green), and MR-RISR (red). Figure 17a shows a large ambiguous mover at approximately 10 m/s (true range of 768 m). All STC cases (3–5) exhibit disambiguation to reveal a low-power mover at approximately 5 m/s that remains masked for Case 2 (Figure 17a). For Cases 3 and 4, the Taylor-tapered processing has a small amount of folded cross-PSF energy that is not present in Case 5 due to optimisation. The MR-RISR estimate produces a super-resolved clutter response at zero Doppler, while both max-SINR and MR-RISR arguably realise a detectable response for the smaller mover for the STC cases (Figure 17b–d).

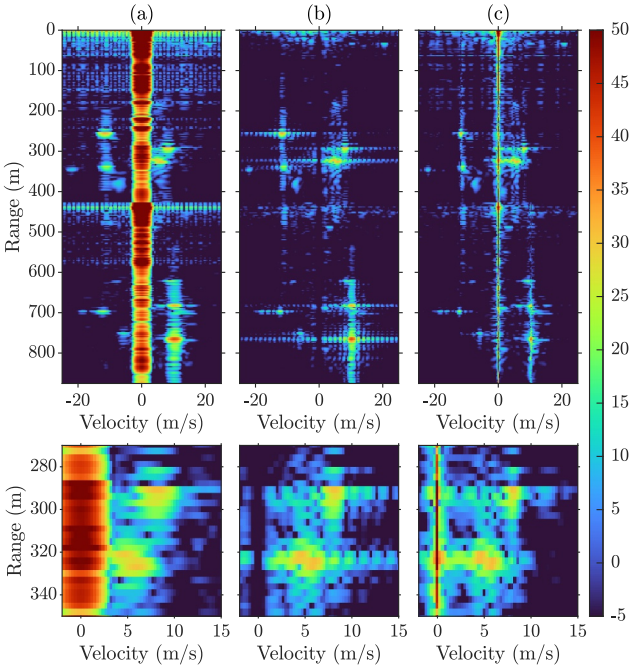

FIGURE 15 | Case 5—Open-air range-Doppler estimates (in dB) using optimised STC (10%) on transmit and $T_p = 3$ μs: (a) Taylor-taper matched filtering, (b) max-SINR filtering, and (c) MR-RISR ($K = 5M$ and 5 iterations). Zoomed-in responses below each figure.

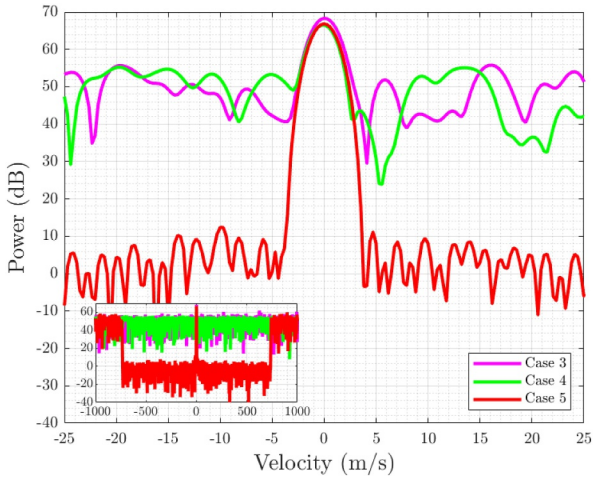

FIGURE 16 | Doppler responses at range cut of 450 m using Taylor-tapered matched filter for Case 3 (pink), Case 4 (green), and Case 5 (red).

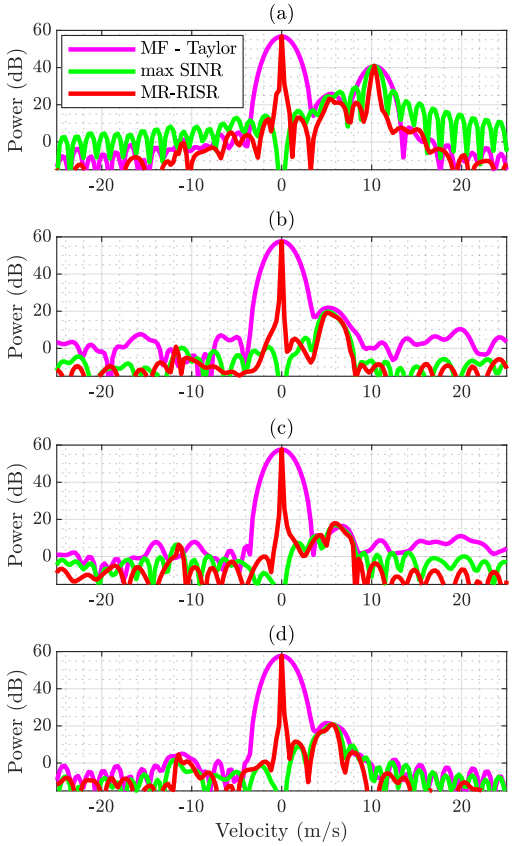

FIGURE 17 | Doppler responses at range cut of 318 m using Taylor-tapered matched filter (pink), max-SINR processing (green), and MR-RISR ($K = 5M$ and five iterations) (red) for (a) Case 2, (b) Case 3, (c) Case 4, and (d) Case 5.

6 | Discussion and Conclusions

Coding of radar pulses in slow-time is a well-known method of range disambiguation. The STC imparts a unique slow-time response onto backscatter, facilitating estimation of scattering from multiple range intervals. For conventional processing (i.e., Doppler matched filtering), the disambiguation performance of STC can be predicted via the cross-PSF. In this work, an STC optimisation routine was introduced that directly minimises the cross-PSF energy for a specified Doppler bandwidth and number of range intervals. The optimisation is effective if the size of the notch (and number of range intervals) is small relative to the unambiguous Doppler extent, and thus is well-suited for applications where scattering is slow-moving and possibly folded in range.

To overcome the limitations of conventional processing, an estimation framework called MR-RISR was also derived. When combined with STC, the adaptive algorithm estimates and isolates scattering from multiple range intervals. MR-RISR is an iterative technique that operates on a single snapshot of data and therefore avoids the issues associated with training data heterogeneity and limited sample support that affect sample-covariance-based estimation. Moreover, the Doppler spectrum estimate exhibits modest super-resolution and effectively suppresses sidelobe energy.

An SINR analysis of conventional, MR-RISR, and clairvoyant max-SINR processing was performed using both random and optimised STC sequences with simulated range-folded scattering. The optimised STC showed the most benefit over a random STC within its optimised notch bandwidth and with conventional processing, while optimisation demonstrated marginal improvements for MR-RISR and max-SINR filtering. Outside of the notched region, the SINR performance degraded for all optimised cases while the random STC SINR loss remained (approximately) flat over Doppler. MR-RISR achieved an SINR loss within about 2–3 dB of the clairvoyant max SINR filter without requiring knowledge of the underlying clutter + noise statistics.

An open-air experiment was conducted to evaluate the range disambiguation performance of the processing methods and random/optimised STCs. Two non-STC CPIs were added to obtain the scattering ground truth and fully ambiguous control cases. It was shown that optimisation of STC is required for conventional Doppler processing to mitigate range-folded sidelobes arising from ambiguous clutter. Further, the STC must be optimised for a notch bandwidth less than the entire Doppler space (but greater than the maximum expected Doppler) to be effective. MR-RISR was shown to have comparable performance to max-SINR filtering with the additional benefit of suppressed target sidelobes and modest super-resolution.

Author Contributions

Jennifer Quirk: conceptualization, data curation, formal analysis, investigation, methodology, software, validation, visualization, writing – original draft, writing – review and editing. **Patrick McCormick:** conceptualization, formal analysis, methodology, software, validation, visualization, writing – original draft, writing – review and editing. **Jonathan Owen:** data curation, investigation, resources, software, validation. **Alfred Fontes:** data curation, investigation, resources. **Shannon Blunt:** conceptualization, funding acquisition, supervision, writing – review and editing.

Funding

This work was supported by the Office of Naval Research under Contract #N00014-23-C-1053. *Distribution Statement A*: Approved for Public Release.

Conflicts of Interest

The authors declare no conflicts of interest.

Data Availability Statement

Research data are not shared.

Endnotes

[1] Range disambiguation performance may also be dependent cross-contamination of range intervals due to spill over of range sidelobes from large targets.

[2] The software-defined radio was set to operate with a 50 MS/s transmit and receive sample rate.

[3] For airborne capture scenarios, the clutter spectrum would need to be estimated via training data [32, 34–37].

[4] Single snapshot methods like MR-RISR are expected to be robust to dynamic clutter behaviour, though the extension to cases involving a moving platform will introduce additional problem complexity due to angle/Doppler coupling [32].

References

1. M. A. Richards, *Fundamentals of Radar Signal Processing*, Vol. 1 (McGraw-Hill, 2005).

2. D. Zrinc and P. Mahapatra, "Two Methods of Ambiguity Resolution in Pulse Doppler Weather Radars," *IEEE Transactions on Aerospace and Electronic Systems* AES-21, no. 4 (1985): 470–483, https://doi.org/10.1109/TAES.1985.310635.

3. M. P. Hartnett, J. T. Clancy, and R. J. Denton, "Utilization of a Nonrecurrent Waveform to Mitigate Range-Folded Spread Doppler Clutter: Application to Over-the-Horizon Radar," *Radio Science* 33, no. 24 (July/August 1998): 1125–1133, https://doi.org/10.1029/98rs01707.

4. J. T. Clancy, H. F. Bascom, and M. P. Hartnett, "Mitigation of Range Folded Clutter by a Nonrecurrent Waveform," in *Proceedings of the 1999 IEEE Radar Conference. Radar into the Next Millennium (Cat. No. 99CH36249)* (April 1999).

5. C. Frush, R. Doviak, M. Sachidananda, and D. Zrnić, "Application of the Sz Phase Code to Mitigate Range–Velocity Ambiguities in Weather Radars," *Journal of Atmospheric and Oceanic Technology* 19, no. 4 (2002): 413–430, https://doi.org/10.1175/1520-0426(2002)019<0413:aotspc>2.0.co;2.

6. N. Levanon, "Mitigating Range Ambiguity in High Prf Radar Using Inter-Pulse Binary Coding," *IEEE Transactions on Aerospace and Electronic Systems* 45, no. 2 (2009): 687–697, https://doi.org/10.1109/taes.2009.5089550.

7. A. De Maio, S. De Nicola, Y. Huang, S. Zhang, and A. Farina, "Code Design to Optimize Radar Detection Performance Under Accuracy and Similarity Constraints," *IEEE Transactions on Signal Processing* 56, no. 11 (2008): 5618–5629, https://doi.org/10.1109/tsp.2008.929657.

8. A. De Maio, S. De Nicola, Y. Huang, Z.-Q. Luo, and S. Zhang, "Design of Phase Codes for Radar Performance Optimization With a Similarity

Constraint," *IEEE Transactions on Signal Processing* 57, no. 2 (2009): 610–621, https://doi.org/10.1109/tsp.2008.2008247.

9. W. W. Lee, *Radar space-time Processing for range-folded spread-Doppler Clutter Mitigation*. PhD dissertation (Duke University, 2011).

10. D. P. Scholnik, "Range-Ambiguous Clutter Suppression With Pulse-Diverse Waveforms," in *2011 IEEE RadarCon (RADAR)*, Vol. MO (May 2011).

11. Q. Cao, G. Zhang, R. D. Palmer, and L. Lei, "Detection and Mitigation of Second-Trip Echo in Polarimetric Weather Radar Employing Random Phase Coding," *IEEE Transactions on Geoscience and Remote Sensing* 50, no. 4 (2012): 1240–1253, https://doi.org/10.1109/tgrs.2011.2164927.

12. A. Aubry, A. DeMaio, A. Farina, and M. Wicks, "Knowledge-Aided (Potentially Cognitive) Transmit Signal and Receive Filter Design in Signal-Dependent Clutter," *IEEE Transactions on Aerospace and Electronic Systems* 49, no. 1 (January 2013): 93–117, https://doi.org/10.1109/taes.2013.6404093.

13. J. B. Mead and A. L. Pazmany, "Quadratic Phase Coding for High Duty Cycle Radar Operation," *Journal of Atmospheric and Oceanic Technology* 36, no. 6 (2019): 957–969, https://doi.org/10.1175/jtech-d-18-0108.1.

14. D. Zrnić and D. Schvartzman, "Phase Codes for Mitigating Ambiguities in Range and Velocity," *Journal of Atmospheric and Oceanic Technology* 38, no. 2 (2021): 313–329, https://doi.org/10.1175/jtech-d-20-0131.1.

15. J. Xiong, G. Cui, T. Fan, et al., "Tangential Maneuvering Target Detection for Airborne Cognitive Radar," *IEEE Transactions on Aerospace and Electronic Systems* 61, no. 1 (February 2025): 401–415, https://doi.org/10.1109/taes.2024.3446960.

16. T. Fan, A. Aubry, V. Carotenuto, A. De Maio, X. Yu, and G. Cui, "Radar Code Design for the Joint Optimization of Detection Performance and Measurement Accuracy in Track Maintenance," *IEEE Transactions on Signal Processing* 73 (2025): 3173–3186, https://doi.org/10.1109/tsp.2025.3587522.

17. S. Unnikrishna Pillai, B. Himed, and K. Y. Li, "Orthogonal Pulsing Schemes for Improved Target Detection in Space Based Radar," in *2005 IEEE Aerospace Conference*, (2005), 2180–2189.

18. S. Pillai, B. Himed, and K. Y. Li, "Effect of Earth's Rotation and Range Foldover on Space-Based Radar Performance," *IEEE Transactions on Aerospace and Electronic Systems* 42, no. 3 (2006): 917–932, https://doi.org/10.1109/taes.2006.248188.

19. BLiP: Beyond Linear Processing, https://www.darpa.mil/program/beyond-linearprocessing.

20. S. D. Blunt, T. Chan, and K. Gerlach, "Robust Doa Estimation: The Reiterative Superresolution (Risr) Algorithm," *IEEE Transactions on Aerospace and Electronic Systems* 47, no. 1 (2011): 332–346, https://doi.org/10.1109/taes.2011.5705679.

21. L. A. Harnett, B. Ravenscroft, S. D. Blunt, and C. T. Allen, "Experimental Evaluation of Adaptive Doppler Estimation for PRI-Staggered Radar," in *2022 IEEE Radar Conference (RadarConf22)* (March 2022).

22. C. C. Jones, Z. E. Gannon, D. DePardo, et al., "Development & Experimental Assessment of Robust Direction Finding and self-calibration," in *2022 IEEE Radar Conference (RadarConf22)* (March 2022).

23. C. C. Jones, Z. E. Gannon, S. D. Blunt, C. T. Allen, and A. F. Martone, "An Adaptive Spectrogram Estimator to Enhance Signal Characterization," in *2022 IEEE Radar Conference (RadarConf22)* (March 2022).

24. S. D. Blunt and K. Gerlach, "Adaptive Pulse Compression via MMSE Estimation," *IEEE Transactions on Aerospace and Electronic Systems* 42, no. 2 (April 2006): 572–584, https://doi.org/10.1109/taes.2006.1642573.

25. T. Higgins, S. D. Blunt, and A. Shackelford, "Time-Range Adaptive Processing for Pulse Agile Radar," in *2010 International Waveform Diversity and Design Conference* (August 2010).

26. J. Harrington, "Challenges and Prospective Solutions for Non-Uniform Radar Waveforms in a Shared Spectrum," in *IEEE Radar Conference (RadarConf24)*, (May 2024).

27. J. E. Quirk, P. M. McCormick, J. W. Owen, and S. D. Blunt, "Experimental Demo of Range Disambiguation via Slow-Time Coding & Reiterative Super-Resolution," in *2024 International Radar Conference*, 2024), 1–5.

28. S. D. Blunt, L. A. Harnett, B. Ravenscroft, R. J. Chang, C. T. Allen, and P. M. McCormick, "Implications of Diversified Doppler for Random PRI Radar," *IEEE Transactions on Aerospace and Electronic Systems* 59, no. 4 (August 2023): 3811–3834, https://doi.org/10.1109/taes.2022.3231844.

29. C. A. Mohr, P. M. McCormick, C. A. Topliff, S. D. Blunt, and J. M. Baden, "Gradient-Based Optimization of PCFM Radar Waveforms," *IEEE Transactions on Aerospace and Electronic Systems* 57, no. 2 (April 2021): 935–956, https://doi.org/10.1109/taes.2020.3037403.

30. D. C. Liu and J. Nocedal, "On the Limited Memory BFGS Method for Large Scale Optimization," *Mathematical Programming* 45, no. 1–3 (August 1989): 503–528, https://doi.org/10.1007/bf01589116.

31. N. Vervliet, O. Debals, L. Sorber, M. V. Barel, and L. D. Lathauwer. "Tensorlab 3.0," Mar, 2016, https://www.tensorlab.net/.

32. J. Ward, *Space-Time Adaptive Processing for Airborne Radar* (Lincoln Laboratory, Massachusetts Institute of Technology, 1994): ESC-TR-94-109.

33. H. L. V. Trees, *Optimum Array Processing: Part IV of Detection, Estimation, and Modulation Theory* (John Wiley & Sons Inc., 2002).

34. I. Reed, J. Mallett, and L. Brennan, "Rapid Convergence Rate in Adaptive Arrays," *IEEE Transactions on Aerospace and Electronic Systems* AES-10, no. 6 (1974): 853–863, https://doi.org/10.1109/taes.1974.307893.

35. D. E. Tyler, "A Distribution-Free m-Estimator of Multivariate Scatter," *Annals of Statistics* (1987): 234–251.

36. F. Gini and M. Greco, "Covariance Matrix Estimation for Cfar Detection in Correlated Heavy Tailed Clutter," *Signal Processing* 82, no. 12 (2002): 1847–1859, https://doi.org/10.1016/s0165-1684(02)00315-8.

37. F. Pascal, Y. Chitour, J.-P. Ovarlez, P. Forster, and P. Larzabal, "Covariance Structure Maximum-Likelihood Estimates in Compound Gaussian Noise: Existence and Algorithm Analysis," *IEEE Transactions on Signal Processing* 56, no. 1 (2007): 34–48, https://doi.org/10.1109/tsp.2007.901652.

38. C. C. Jones, L. A. Harnett, C. A. Mohr, S. D. Blunt, and C. T. Allen, "Structure-Based Adaptive Radar Processing for Joint Clutter Cancellation and Moving Target Estimation," in *IEEE International Radar Conference* (April 2020).

39. S. Blunt and K. Gerlach, "Multistatic Adaptive Pulse Compression," *IEEE Transactions on Aerospace and Electronic Systems* 42, no. 3 (2006): 891–903, https://doi.org/10.1109/taes.2006.248196.

40. L. A. Harnett, B. Ravenscroft, D. G. Felton, P. M. McCormick, J. W. Owen, and S. D. Blunt, "Adaptive Doppler Estimation for Random PRI Staggering With Clutter Cancellation," *IEEE Transactions on Radar Systems* 4, no. Feb (2026): 564–585, https://doi.org/10.1109/trs.2026.3664255.

41. K. B. Petersen and M. S. Pedersen, The Matrix Cookbook, (November 2012).

42. T. Higgins, S. D. Blunt, and K. Gerlach, "Gain-Constrained Adaptive Pulse Compression via an Mvdr Framework," in *2009 IEEE Radar Conference*, (2009), 1–6.

Appendix A

Gradient of Equation (24)

For an arbitrary $N \times 1$ vector $\mathbf{x}$, the partial derivative with respect to each element is defined as

$$\frac{\partial}{\partial \mathbf{x}} = \begin{bmatrix} \frac{\partial}{\partial x_1} & \frac{\partial}{\partial x_2} & \cdots & \frac{\partial}{\partial x_N} \end{bmatrix}^T. \tag{A1}$$

Likewise, for an arbitrary $N \times M$ matrix $\mathbf{X}$, the partial derivative with respect to each element is defined as

$$\frac{\partial}{\partial \mathbf{X}} = \begin{bmatrix} \frac{\partial}{\partial x_{11}} & \frac{\partial}{\partial x_{12}} & \cdots & \frac{\partial}{\partial x_{1M}} \\ \frac{\partial}{\partial x_{21}} & \frac{\partial}{\partial x_{22}} & \cdots & \frac{\partial}{\partial x_{2M}} \\ \vdots & \vdots & \ddots & \vdots \\ \frac{\partial}{\partial x_{N1}} & \frac{\partial}{\partial x_{N2}} & \cdots & \frac{\partial}{\partial x_{NM}} \end{bmatrix}. \tag{A2}$$

The traditional approach to solving a gradient involves writing the cost function in terms of a series of summations (Einsteinian notation) and determining the partial derivatives for each element. Since the cost function considered here is rather complicated, we can leverage the Jacobian

$$\mathbf{\Phi}_{\mathbf{xy}} = \begin{bmatrix} \frac{\partial y_1}{\partial x_1} & \frac{\partial y_2}{\partial x_1} & \cdots & \frac{\partial y_M}{\partial x_1} \\ \frac{\partial y_1}{\partial x_2} & \frac{\partial y_2}{\partial x_2} & \cdots & \frac{\partial y_M}{\partial x_2} \\ \vdots & \vdots & \ddots & \vdots \\ \frac{\partial y_1}{\partial x_N} & \frac{\partial y_2}{\partial x_N} & \cdots & \frac{\partial y_M}{\partial x_N} \end{bmatrix}, \tag{A3}$$

which contains the partial derivatives of each element in the $M \times 1$ vector $\mathbf{y}$ with respect to each element in $\mathbf{x}$. Supposing $\mathbf{y} = f(\mathbf{x})$, the Jacobian acts as a linear transformation between the partial derivative with respect to $\mathbf{y}$ and the partial derivative with respect to $\mathbf{x}$ as

$$\frac{\partial}{\partial \mathbf{x}} = \mathbf{\Phi}_{\mathbf{xy}} \frac{\partial}{\partial \mathbf{y}}. \tag{A4}$$

This Jacobian relationship is fundamental for using the chain rule to break down a complicated cost function. Derivatives involving matrices also implicitly follow from Equation (A4) due to the identity $\text{vec}\{\mathbf{XYZ}\} = (\mathbf{Z}^T \otimes \mathbf{X})\text{vec}\{\mathbf{Y}\}$, where $\mathbf{Y}$ and $\mathbf{Z}$ are arbitrary matrices having dimensions conducive to multiplication with $\mathbf{X}$ and each other, $\otimes$ denotes the Kronecker product, and $\text{vec}\{\bullet\}$ is the vectorisation operation [41]. Particularly helpful derivative identities include the chain rule for elementwise operations, the matrix multiplication chain rule, and the complex chain rule.

First, for $\mathbf{Z} = \mathbf{X} \odot \mathbf{Y}$, the chain rule for elementwise operations is given by

$$\frac{\partial}{\partial \mathbf{Y}} = \mathbf{X} \odot \frac{\partial}{\partial \mathbf{Z}}. \tag{A5}$$

If we instead let $\mathbf{Z} = \mathbf{XY}$, then the matrix multiplication chain rule is defined as

$$\frac{\partial}{\partial \mathbf{Y}} = \mathbf{X}^T \frac{\partial}{\partial \mathbf{Z}}. \tag{A6}$$

Finally, supposing $\mathbf{Y} = f(\mathbf{X})$, the complex chain rule is given by

$$\frac{\partial}{\partial \mathbf{X}} = \frac{\partial}{\partial \mathbf{Y}} \frac{\partial \mathbf{Y}}{\partial \mathbf{X}} + \frac{\partial}{\partial \mathbf{Y}^*} \frac{\partial \mathbf{Y}^*}{\partial \mathbf{X}}. \tag{A7}$$

To leverage Equation (A4), we begin by defining a sequence of intermediate variables in Table A1, noting the operation-by-operation progression 'inward' of Equation (24) when moving down the rows of the table.

TABLE A1 | Intermediate variable definitions from Equation (24).

$J = \alpha^{1/p}$
$\alpha = \sum_{b=1}^{G-1} \sum_{a=0}^{b-1} \beta_{a,b}$
$\beta_{a,b} = \mathbf{1}^T \boldsymbol{\gamma}_{a,b}$
$\boldsymbol{\gamma}_{a,b} = \lvert \mathbf{c}_{a,b} \rvert^p$
$\mathbf{c}_{a,b} = \mathbf{e} \odot \mathbf{f}_{a,b}$
$\mathbf{f}_{a,b} = \mathbf{G}_{a,b} \mathbf{d}(\theta)$
$\mathbf{G}_{a,b} = \mathbf{H}_b \mathbf{T}_a$
$\mathbf{H}_b = \mathbf{V}^H \odot \mathbf{K}_b^H$
$\mathbf{K}_b = \mathbf{T}_b \mathbf{L}$
$\mathbf{L} = \mathbf{d}^*(\theta) \mathbf{1}^T$
$\mathbf{d}(\theta) = e^{j\theta}$

The partial derivatives of J from Equation (24) with respect to each variable defined in Table A1 are given in Table A2, where the relevant derivative identity for each step is stated in the rightmost column. The intermediate variables from the fourth row until the end of the table yield two separate partial derivatives since Wirtinger calculus treats each variable and its conjugate as independent. Also recall that $\mathbf{e}$ and the $\mathbf{T}_g$ are entirely real.

To obtain the gradient of J with respect to θ, we start with $\partial J / \partial \theta^*$ as given by the last row of Table A2 and perform substitutions when applicable. Note that $\partial J / \partial \mathbf{d}^*(\theta)$ includes two double summation terms since $\mathbf{d}(\theta)$ appears in both $\mathbf{f}_{a,b}$ and $\mathbf{L}$.

Appendix B

Derivation of Equation (34)

The gain constrained formulation follows the steps discussed in [42]. These steps are repeated here for completeness using the STC signal model. The Lagrangian representation of Equation (33) can be expressed as

$$\mathcal{L}(\mathbf{w}_{g,k}) = \mathbb{E}\left[|x_{g,k} - \mathbf{w}_{g,k}^H \mathbf{z}|^2\right] - 2\Re\left\{\lambda\left(\mathbf{w}_{g,k}^H \mathbf{v}_{g,k} - 1\right)\right\}, \tag{A8}$$

where λ is a complex-valued Lagrange multiplier, $\Re\{\bullet\}$ extracts the real-valued component, $\mathbf{w}_{g,k} = \mathbf{w}_g(\bar{\tau}, f_{\mathrm{D},k})$, $x_{g,k} = x_g(\bar{\tau}, f_{\mathrm{D},k})$, and the functional dependence on f_{D} and $\bar{\tau}$ is suppressed for brevity.

Taking the gradient of $\mathcal{L}(\mathbf{w}_{g,k})$ with respect to $\mathbf{w}_{g,k}$ yields

$$\frac{\partial \mathcal{L}(\mathbf{w}_{g,k})}{\partial \mathbf{w}_{g,k}} = -\mathbb{E}\left[x_{g,k}^* \mathbf{z}\right] + \mathbb{E}\left[\mathbf{z}\mathbf{z}^H\right]\mathbf{w}_{g,k} - \lambda^* \mathbf{v}_{g,k}. \tag{A9}$$

Setting the gradient equal to zero and solving for $\mathbf{w}_{g,k}$ provides

$$\mathbf{w}_{g,k} = \mathbf{R}^{-1}\left(\mathbf{p}_{g,k} + \lambda^* \mathbf{v}_{g,k}\right), \tag{A10}$$

where $\mathbf{R} = \mathbb{E}\left[\mathbf{z}\mathbf{z}^H\right]$ and $\mathbf{p}_{g,k} = \mathbb{E}\left[x_{g,k}^* \mathbf{z}\right]$. The Lagrange multiplier λ can be determined by incorporating the form of $\mathbf{w}_{g,k}$ into the linear constraint $\mathbf{w}_{g,k}^H \mathbf{v}_{g,k} = 1$. Solving for λ then yields

$$\lambda = \frac{1 - \mathbf{p}_{g,k}^H \mathbf{R}^{-1} \mathbf{v}_{g,k}}{\mathbf{v}_{g,k}^H \mathbf{R}^{-1} \mathbf{v}_{g,k}}. \tag{A11}$$

Plugging the expression for λ back into the form for $\mathbf{w}_{g,k}$ results in

$$\mathbf{w}_{g,k} = \frac{\mathbf{R}^{-1}\mathbf{v}_{g,k}}{\mathbf{v}_{g,k}^H \mathbf{R}^{-1}\mathbf{v}_{g,k}} + \mathbf{R}^{-1}\mathbf{p}_{g,k} - \left(\frac{\mathbf{p}_{g,k}^H \mathbf{R}^{-1}\mathbf{v}_{g,k}}{\mathbf{v}_{g,k}^H \mathbf{R}^{-1}\mathbf{v}_{g,k}}\right)\mathbf{R}^{-1}\mathbf{v}_{g,k}. \tag{A12}$$

The forms for $\mathbf{R}$ and $\mathbf{p}_{g,k}$ can be simplified via correlation assumptions on the scattering. Denoting $\mathbf{x}_g = \mathbf{x}_g(\bar{\tau})$, there are four main assumptions: (1) all noise and scattering is zero mean, $\mathbb{E}\left[\mathbf{x}_g\right] = \mathbf{0}_{K\times 1}$ and $\mathbb{E}[\mathbf{u}] = \mathbf{0}_{M\times 1}$; (2) scattering from different range intervals is uncorrelated, $\mathbb{E}\left[\mathbf{x}_g \mathbf{x}_{g'}^H\right] = \mathbf{0}_{K\times K}$ for $g \neq g'$; (3) noise is uncorrelated with scattering, $\mathbb{E}\left[\mathbf{x}_g \mathbf{u}^H\right] = \mathbf{0}_{K\times M}$; and (4) scattering across Doppler and within a range interval is uncorrelated (except with itself). Defining $\mathbf{P}_g = \mathbb{E}\left[\mathbf{x}_g \mathbf{x}_g^H\right]$, the last assumption becomes

$$\left[\mathbf{P}_g\right]_{kk'} = \begin{cases} \mathbb{E}\left[|x_{g,k}|^2\right] & k = k' \\ 0 & \text{otherwise} \end{cases}, \tag{A13}$$

where $\left[\mathbf{P}_g\right]_{kk'}$ the $(k, k')^{\text{th}}$ entry in the $K \times K$ matrix. Leveraging the form of $\mathbf{z}$ from Equation (30) and applying these assumptions, $\mathbf{R}$ becomes a structured matrix

$$\begin{aligned} \mathbf{R} &= \mathbb{E}\left[\mathbf{z}\mathbf{z}^H\right] \\ &= \mathbb{E}\left[\left(\sum_{g=0}^{G-1} \mathbf{V}_g \mathbf{x}_g + \mathbf{u}\right)\left(\sum_{g=0}^{G-1} \mathbf{V}_g \mathbf{x}_g + \mathbf{u}\right)^H\right] \\ &= \sum_{g=0}^{G-1} \mathbf{V}_g \mathbf{P}_g \mathbf{V}_{g'}^H + \mathbf{R}_{\mathrm{u}}, \end{aligned} \tag{A14}$$

where $\mathbf{R}_{\mathrm{u}} = \mathbb{E}\left[\mathbf{u}\mathbf{u}^H\right]$ is the noise covariance, and vector $\mathbf{p}$ becomes

$$\begin{aligned} \mathbf{p}_{g,k} &= \mathbb{E}\left[x_{g,k}^* \mathbf{z}\right] \\ &= \mathbb{E}\left[x_{g,k}^*\left(\sum_{g=0}^{G-1} \mathbf{V}_g \mathbf{x}_g + \mathbf{u}\right)\right] \\ &= \mathbb{E}\left[|x_{g,k}|^2\right]\mathbf{v}_{g,k}. \end{aligned} \tag{A15}$$

Plugging Equations (A14) and (A15) into Equation (A12) yields the form from Equation (34).

TABLE A2 | Step-by-step partial derivatives for intermediate variables.

Intermediate variable	Derivatives		Derivative rule
$J = \alpha^{1/p}$	$\frac{\partial J}{\partial \alpha} = \frac{1}{p}\alpha^{1/p-1}$		Power rule
$\alpha = \sum_{b=1}^{G-1}\sum_{a=0}^{b-1} \beta_{a,b}$	$\frac{\partial J}{\partial \beta_{a,b}} = \frac{\partial J}{\partial \alpha}$		Chain rule
$\beta_{a,b} = \mathbf{1}^T \boldsymbol{\gamma}_{a,b}$	$\frac{\partial J}{\partial \boldsymbol{\gamma}_{a,b}} = \mathbf{1}\frac{\partial J}{\partial \beta_{a,b}}$		Equation (A6)
$\boldsymbol{\gamma}_{a,b} = \lvert\mathbf{c}_{a,b}\rvert^p$	$\frac{\partial J}{\partial \mathbf{c}_{a,b}} = p\lvert\mathbf{c}_{a,b}\rvert^{p-2} \odot \mathbf{c}_{a,b}^* \odot \frac{\partial J}{\partial \boldsymbol{\gamma}_{a,b}}$	$\frac{\partial J}{\partial \mathbf{c}_{a,b}^*} = p\lvert\mathbf{c}_{a,b}\rvert^{p-2} \odot \mathbf{c}_{a,b} \odot \frac{\partial J}{\partial \boldsymbol{\gamma}_{a,b}}$	Power rule, Equations (A5) and (A7)
$\mathbf{c}_{a,b} = \mathbf{e} \odot \mathbf{f}_{a,b}$	$\frac{\partial J}{\partial \mathbf{f}_{a,b}} = \mathbf{e} \odot \frac{\partial J}{\partial \mathbf{c}_{a,b}}$	$\frac{\partial J}{\partial \mathbf{f}_{a,b}^*} = \mathbf{e} \odot \frac{\partial J}{\partial \mathbf{c}_{a,b}^*}$	Equations (A5) and (A7)
$\mathbf{f}_{a,b} = \mathbf{G}_{a,b}\mathbf{d}(\theta)$	$\frac{\partial J}{\partial \mathbf{G}_{a,b}} = \frac{\partial J}{\partial \mathbf{f}_{a,b}}\mathbf{d}^T(\theta)$	$\frac{\partial J}{\partial \mathbf{G}_{a,b}^*} = \frac{\partial J}{\partial \mathbf{f}_{a,b}^*}\mathbf{d}^H(\theta)$	Equations (A6) and (A7)
$\mathbf{G}_{a,b} = \mathbf{H}_b\mathbf{T}_a$	$\frac{\partial J}{\partial \mathbf{H}_b} = \frac{\partial J}{\partial \mathbf{G}_{a,b}}\mathbf{T}_a^T$	$\frac{\partial J}{\partial \mathbf{H}_b^*} = \frac{\partial J}{\partial \mathbf{G}_{a,b}^*}\mathbf{T}_a^T$	Equations (A6) and (A7)
$\mathbf{H}_b = \mathbf{V}^H \odot \mathbf{K}_b^H$	$\frac{\partial J}{\partial \mathbf{K}_b} = \mathbf{V} \odot \left(\frac{\partial J}{\partial \mathbf{H}_b}\right)^T$	$\frac{\partial J}{\partial \mathbf{K}_b^*} = \mathbf{V}^* \odot \left(\frac{\partial J}{\partial \mathbf{H}_b^*}\right)^T$	Equations (A5) and (A7)
$\mathbf{K}_b = \mathbf{T}_b\mathbf{L}$	$\frac{\partial J}{\partial \mathbf{L}} = \mathbf{T}_b^T\frac{\partial J}{\partial \mathbf{K}_b}$	$\frac{\partial J}{\partial \mathbf{L}^*} = \mathbf{T}_b^T\frac{\partial J}{\partial \mathbf{K}_b^*}$	Equations (A6) and (A7)
$\mathbf{L} = \mathbf{d}^*(\theta)\mathbf{1}^T$	$\frac{\partial J}{\partial \mathbf{d}(\theta)} = \sum_{r=1}^{G-1}\sum_{q=0}^{r-1}\frac{\partial J}{\partial \mathbf{L}^*}\mathbf{1} + \sum_{r=1}^{G-1}\sum_{q=0}^{r-1}\mathbf{G}_{q,r}^T\frac{\partial J}{\partial \mathbf{f}_{q,r}}$	$\frac{\partial J}{\partial \mathbf{d}^*(\theta)} = \sum_{r=1}^{G-1}\sum_{q=0}^{r-1}\frac{\partial J}{\partial \mathbf{L}}\mathbf{1} + \sum_{r=1}^{G-1}\sum_{q=0}^{r-1}\mathbf{G}_{q,r}^H\frac{\partial J}{\partial \mathbf{f}_{q,r}^*}$	Equations (A6) and (A7)
$\mathbf{d}(\theta) = e^{j\theta}$	$\frac{\partial J}{\partial \theta} = -2\Im\left\{\mathbf{d}(\theta) \odot \frac{\partial J}{\partial \mathbf{d}(\theta)}\right\}$	$\frac{\partial J}{\partial \theta^*} = 2\Im\left\{\mathbf{d}^*(\theta) \odot \frac{\partial J}{\partial \mathbf{d}^*(\theta)}\right\}$	Equation (A7)